Integrated interpretation of helicopter and ground-based geophysical data recorded within the Okavango Delta, Botswana

CrossMark

Joel E. Podgorski [a,*], Alan G. Green [a], Thomas Kalscheuer [a,b], Wolfgang K.H. Kinzelbach [c], Heinrich Horstmeyer [a], Hansruedi Maurer [a], Lasse Rabenstein [a], Joseph Doetsch [a], Esben Auken [d], Tiyapo Ngwisanyi [e], Gomotsang Tshoso [e], Bashali Charles Jaba [e], Onkgopotse Ntibinyane [e], Kebabonye Laletsang [f]

[a] Institute of Geophysics, ETH, Sonneggstr. 5, 8092 Zurich, Switzerland
[b] Uppsala University, Department of Earth Sciences, Villavägen 16 B, 752 36 Uppsala, Sweden
[c] Institute of Environmental Engineering, Wolfgang-Pauli-Str. 15, 8093 Zürich, Switzerland
[d] Institute for Geoscience, Aarhus University, C F Moellers Allé 4, DK-8000 Aarhus C, Denmark
[e] Department of Geological Survey, Private Bag 14, Lobatse, Botswana
[f] Department of Geology, University of Botswana, Private Bag UB00704, Gaborone, Botswana

ARTICLE INFO

ABSTRACT

Integration of information from the following sources has been used to produce a much better constrained and more complete four-unit geological/hydrological model of the Okavango Delta than previously available: (i) a 3D resistivity model determined from helicopter time-domain electromagnetic (HTEM) data recorded across most of the delta, (ii) 2D models and images derived from ground-based electrical resistance tomographic, transient electromagnetic, and high resolution seismic reflection/refraction tomographic data acquired at four selected sites in western and north-central regions of the delta, and (iii) geological details extracted from boreholes in northeastern and southeastern parts of the delta. The upper heterogeneous unit is the modern delta, which comprises extensive dry and freshwater-saturated sand and lesser amounts of clay and salt. It is characterized by moderate to high electrical resistivities and very low to low P-wave velocities. Except for images of several buried abandoned river channels, it is non-reflective. The laterally extensive underlying unit of low resistivities, low P-wave velocity, and subhorizontal reflectors very likely contains saline-water-saturated sands and clays deposited in the huge Paleo Lake Makgadikgadi (PLM), which once covered a 90,000 km^2 area that encompassed the delta, Lake Ngami, the Mababe Depression, and the Makgadikgadi Basin. Examples of PLM sediments are intersected in many boreholes. Low permeability clay within the PLM unit seems to be a barrier to the downward flow of the saline water. Below the PLM unit, freshwater-saturated sand of the Paleo Okavango Megafan (POM) unit is distinguished by moderate to high resistivities, low P-wave velocity, and numerous subhorizontal reflectors. The POM unit is interpreted to be the remnants of a megafan based on the arcuate nature of its front and the semi-conical shape of its upper surface in the HTEM resistivity model. Moderate to high resistivity subhorizontal layers are consistent with this interpretation. The deepest unit is the basement with very high resistivity, high P-wave velocity, and low or complex reflectivity. The interface between the POM unit and basement is a prominent seismic reflector.

1. Introduction

The Okavango Delta is a largely pristine wilderness wetland near the terminus of one of Africa's longest undammed river systems (Fig. 1a). It is an important habitat for numerous plant and animal species in the middle of the otherwise harsh environment of the semi-arid Kalahari Desert. Though commonly referred to as an inland delta, most of it is an alluvial megafan (Fig. 2a; Stanistreet and McCarthy, 1993; Burke and Gunnell, 2008; McCarthy, 2013). In the following, we refer to deltas at the edges of lakes as well as water-covered megafans that have not always terminated at lakes (i.e., the current Okavango Delta) as deltas.

To investigate the poorly known geology and hydrogeology of the Okavango Delta, the government of Botswana commissioned three helicopter transient electromagnetic (HTEM) surveys: a regional survey of the delta (panhandle and megafan in Fig. 2a) and high resolution surveys of two targeted regions of the delta. To allow the data to be meaningfully inverted, it was necessary to pass them through a novel editing, calibration, and processing scheme. Details on this scheme and the initial results of inverting one of the processed high resolution HTEM data sets were presented by Podgorski et al. (2013a), and a highly simplified resistivity model obtained from inverting the processed regional

* Corresponding author.
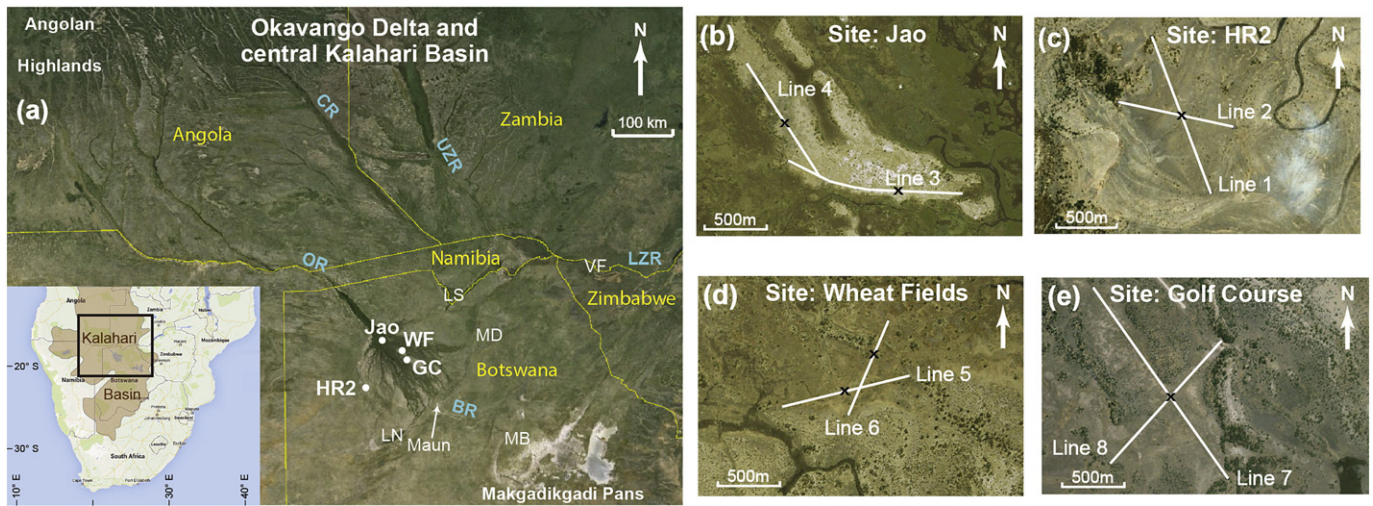 E-mail address: joel.podgorski@erdw.ethz.ch (J.E. Podgorski).

Fig. 1. (a) Okavango Delta in northern Botswana and locations of the four ground-based geophysical study sites: HR2, Jao, WF (Wheat Fields), and GC (Golf Course). BR — Boteti River; CR — Cuando River; LN — Lake Ngami; LS — Linyanti Swamps; LZR — Lower Zambezi River; MB — Makgadikgadi Basin; MD — Mababe Depression; OR — Okavango River; UZR — Upper Zambezi River; VF — Victoria Falls. Inset shows a large part of the Kalahari Basin (after Thomas and Shaw, 1991) and location of main map within southern Africa. ERT, TEM, and seismic reflection/refraction tomographic survey lines at (b) Jao in the upper-central megafan, (c) HR2 in the western megafan, and (d) and (e) Wheat Fields and Golf Course on Chief's Island. Black x's indicate centre points of ERT surveys and the coordinate origin of all ground-based surveys.
Satellite images from Google Earth (©2013 Google).

HTEM data set was first described in a short article by Podgorski et al. (2013b).

The regional HTEM resistivity model contained four distinct layers (i.e., three layers and a half-space) or units. Podgorski et al. (2013b) interpreted the upper unit in terms of sediments deposited in the modern Okavango Delta and speculated that the two successively deeper units represented sediments deposited in a huge paleo lake (Paleo Lake Makgadikgadi — PLM) and a paleo megafan/large inland delta (Paleo Okavango Megafan — POM), respectively. The deepest unit (i.e., half space) was interpreted as basement.

To improve our knowledge of these units, we acquired ground-based electrical resistance tomographic (ERT), transient electromagnetic (TEM), and high resolution seismic reflection/refraction tomographic data at four sites (Fig. 1) carefully chosen to help constrain the interpretation of the HTEM model. Resistivity models derived from the ERT and the

TEM data recorded at the HR2 and Jao sites have been presented by Meier et al. (2014), and P-wave velocity models and seismic reflection images derived from the seismic data collected at the same two sites have been presented by Reiser et al. (2014). Preliminary versions of these models and images helped guide Podgorski et al.'s (2013b) tentative interpretation.

Since Podgorski et al. (2013a,b), Meier et al. (2014), and Reiser et al. (2014) were submitted for publication, we have inverted the ERT, TEM and seismic refraction data recorded at all four sites using common regularization parameters for each type of data. The uniform regularization used in the inversions of the ERT and the uniform regularization used in the inversions of the TEM data were chosen to produce "optimum" results at the four sites. As a result, the regularization parameters used for our inversions of the ERT and TEM data at HR2 and Jao (Fig. 1) were slightly different from those used by Meier et al. (2014). However,
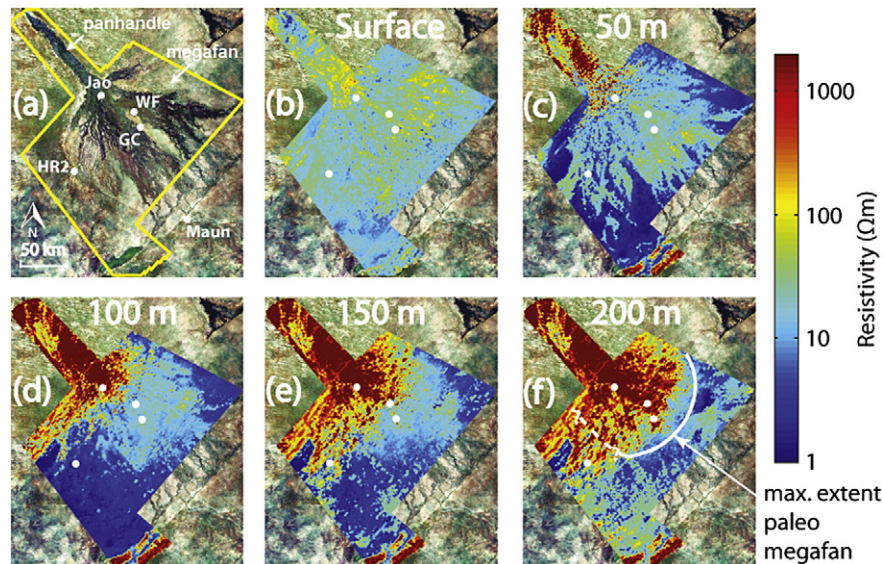

Fig. 2. (a) Outline of HTEM survey area with dots showing locations of the four ground-based geophysical study sites. The HTEM survey was flown with 2-km-line spacing in a SW-NE direction. (b)–(f) Resistivity depth slices extracted from the final model of the regional HTEM data. The proposed paleo megafan is discussed in the text.

our resistivity models for these two sites are similar to and consistent with the respective models of Meier et al. (2014). We have also applied a common processing scheme to all seismic reflection data.

In this contribution, we present ERT- and TEM-based resistivity models and combined P-wave tomographic velocity and seismic reflection images for the four sites, all of which have been derived using uniform procedures and parameters. We also present the first comprehensive integrated interpretation based on all airborne and ground-based geophysical models and images and on geological information obtained from borehole logs.

The resistivity models for the two new sites, Wheat Fields and Gulf Course, are particularly important because (i) they are well constrained, (ii) the respective data sets were collected across typical moderate to high resistivity near-surface sediments of the Okavango Delta, and (iii) both sites are situated above the proposed POM, one of the primary targets of the ground-based investigations. The model obtained from the Golf Course TEM data provides the first reasonably well-determined estimate of POM resistivity, thus supplying critical support for the POM hypothesis. In contrast, HR2 lies outside the boundaries of POM and Jao is located within a small anomalous region of low resistivity near-surface sediments. Furthermore, we have low confidence in the resistivity models derived from the ERT and TEM data recorded across Jao, a small island surround by fresh water.

We begin with a brief overview of the Okavango Delta and an outline of information provided by previous geophysical surveys, including the HTEM surveys. After describing the ground-based field sites and the employed geophysical methods, we present our results and discuss their implications for the evolution of the region.

2. Okavango Delta

The Okavango Delta lies within the Kalahari Basin, which attained its relatively high average elevation of >900 m during the break-up of Gondwana (Cox, 1989). Subsequent tectonism, erosion, and sedimentation resulted in a huge flat sand-covered area bounded by crustal swells (Burke and Gunnell, 2008). The relevant part of the Kalahari Basin for our study extends from the Angolan Highlands in the northwest to the Makgadikgadi Pans in the southeast (inset to Fig. 1a; Thomas and Shaw, 1991). It is reported to contain several hundred metres of lacustrine, fluvial, and aeolian sediments (Thomas and Shaw, 1991; Haddon and McCarthy, 2005).

Extensive Cainozoic tectonism and climate change caused major reorganizations of river systems throughout the basin, including severance of the paleo Okavango and paleo Limpopo rivers and capture of former southward-flowing Zambezi River tributaries (Du Toit, 1927; Thomas and Shaw, 1988; Moore and Larkin, 2001; Moore et al., 2012; McCarthy, 2013). These events were responsible for different stages of PLM, which ranged in elevation from 912–945 m (Cooke, 1980; Thomas and Shaw, 1991; Moore et al., 2012). Various studies (Burrough et al., 2009a and references therein) have established that PLM once covered a 66,000 km² area southeast and northeast of the delta.

The gradient of the Okavango Delta surface at the present time is very low with an elevation drop of only ~60 m over its ~250 km length (McCarthy et al., 1997; Gumbricht et al., 2005). The comparatively narrow panhandle comprises lagoons and meandering channels that flow into the broad megafan of river channels, swamps, and islands (Fig. 2a). Channels are in a continuous state of flux due to active tectonism, sedimentation, vegetation growth, and animal movements (McCarthy et al., 1986, 1993, 1998b). Rivers connect the megafan with Lake Ngami, the Mababe Depression, the Linyanti Swamps, and the Makgadikgadi Pans (Fig. 1a).

Most of the delta is characterized by thick freshwater aquifers overlying saline-water aquifers (McCarthy et al., 1998a; Milzow et al., 2009). Its hydrology is strongly influenced by an annual flood controlled by water that precipitates hundreds of kilometres away in the Angolan Highlands. After flowing through a network of streams and rivers, this water is eventually brought into the delta by the Okavango River (Fig. 1a). The distant precipitation supplies 60% of the water influx to the delta with the remainder originating from direct rainfall (Milzow et al., 2009). The 3300–10,400 km² of seasonal floodplains augments the ~3300 km² of land perennially covered by water (McCarthy, 2013).

Currently, fluvial, chemical, and atmospheric processes are mainly responsible for sedimentation within the delta (Garstang et al., 1998; Milzow et al., 2009; McCarthy, 2013). The fluvial sediments are a combination of particles (~200,000 tonnes/year) and solutes (~400,000 tonnes/year) transported by the Okavango River. Most of the particle sediments are sand deposited in river channels. In contrast, most of the solutes precipitate as large volumes of salt, calcretes, and silcretes on and around islands and drying floodplains via evapotranspiration of river water that enters shallow aquifers along wetland margins. The annual quantity of atmospheric-transported sediments (i.e., aeolian sand and aerosols) distributed across the delta is not well known, but is expected to be substantial.

Evapotranspiration is responsible for nearly all of the water leaving the delta; McCarthy (2006, 2013) estimates that only ~2% of the inflowing water eventually exits by surface flow and a minimal amount via groundwater flow. In spite of this, the solute content of the surface waters is uniformly low from the upper panhandle (40 ppm) in the northwest to near the city of Maun (80 ppm) in the southeast (McCarthy et al., 1998a). One mechanism proposed to explain the continued freshness of the surface waters is salt fingering, whereby density instabilities cause plumes of the surface and near-surface salt accumulations to sink towards the saline-water aquifers (McCarthy and Ellery, 1994; Gieske, 1996; Milzow et al., 2009).

Incomplete information on past sedimentation is provided by a 90-m-deep borehole within the northeastern part of the delta (Bauer, 2004) and numerous boreholes along the southeastern extremity of the delta, some of which are 170–180 m deep (MMEWR, 2004). None of these boreholes reach basement. Boreholes along the edges of the delta and scattered seismic refraction surveys within it (Greenwood and Carruthers, 1973; Podgorski et al., 2013b; Reiser et al., 2014) supply a limited number of reliable total sediment thickness estimates (50–360 m), and Euler deconvolution of aeromagnetic data (Modisi et al., 2000; Kinabo et al., 2007, 2008; Brunner et al., 2007) yields information on relative changes in total sediment thickness. Geological maps derived from aeromagnetic-based interpolations and extrapolations of basement rocks observed outside of the delta at sparse outcrops and in a few boreholes suggest that the delta sediments are underlain by Precambrian and Karoo rocks (Key and Ayers, 2000; Kinabo et al., 2008).

The panhandle lies within a northwest–southeast trending graben, whereas the megafan is situated within a northeast–southwest trending half-graben. There are several hundred metres of displacement on faults along the southeastern edge of the half-graben (Kinabo et al., 2007, 2008; Podgorski et al., 2013b). This half-graben, which is seismically active (Fairhead and Girdler, 1971; Reeves, 1972; Hutchison and Midgley, 1973), is interpreted to be a southwesterly extension of the East Africa Rift System (Du Toit, 1927; Scholz et al., 1976; Thomas and Shaw, 1991; Modisi et al., 2000).

3. HTEM survey

Originally developed for mineral exploration, the HTEM method is being increasingly used for investigations of low-contrast hydrogeological targets (Auken et al., 2006; Christiansen et al., 2009; Steuer et al., 2009; Kirkegaard et al., 2011; Siemon et al., 2011; Jørgensen et al., 2012; Podgorski et al., 2013b). It is a cost effective means of rapidly surveying the subsurface resistivity of large areas.

The regional HTEM survey of the Okavango Delta covered the panhandle and megafan with a 2-km-line spacing (Fig. 2a). The 15,000 line-km of recorded data were inverted using Auken and Christiansen's (2004) pseudo-2D scheme. The two targeted areas within the delta

(HR1 — 5 × 5 km; HR2 — 5 × 7 km) were surveyed using a much closer line spacing of 50 m and inverted using Viezzoli et al.'s (2008) pseudo-3D scheme. Practically all of the HTEM data were of exceptionally high quality, mainly because electromagnetic noise within the delta was very low and there were strong contrasts in the electrical resistivities of the various geological elements.

Models based on the high resolution HR1 and HR2 data are fully compatible with models based on the regional data (Podgorski et al., 2013a; Meier et al., 2014). For this reason, the high resolution data sets and models will not be discussed here. Further details on the HTEM survey specifications, data processing, and inversions can be found in Podgorski et al. (2013a).

Inversions of the HTEM data yield resistivity models distinguished by three principal layers and a half-space (Fig. 2b–f; Podgorski et al., 2013b). An average ~50-m-thick moderately to highly resistive surface layer is underlain sequentially by an average ~100-m-thick conductive layer and one or more higher resistivity layers. The heterogeneous surface layer is mostly attributable to the open surface waters and dry and freshwater-saturated sand. Podgorski et al. (2013b) interpret the underlying conductive layer to be a northwesterly extension of PLM sediments, primarily on the basis of information provided by boreholes (Bauer, 2004; MMEWR, 2004; T. Preston, personal communication, 2010). Since no boreholes have sampled the deeper higher resistivity layer, its interpretation is more speculative. The fan shape of the deep higher resistivities is a distinctive aspect of the HTEM model in Fig. 2e and f. Although deep higher resistivities are required by the late-time-gate data and the depth to the base of the conductive layer is mostly well resolved in the HTEM models, the numerical resistivity estimates of the immediately underlying layer and half-space are poorly determined. As a consequence, the fan-shaped resistive feature could be either freshwater-saturated sand deposited in a paleo megafan (i.e., POM)/paleo inland delta with moderate resistivities or basement rock with high resistivities. A primary goal of the ground-based geophysical measurements described below was to resolve this ambiguity.

4. Field sites

One of the four ground-based field sites was located within the HR2 survey area along the western edge of the delta, some distance from the interpreted POM unit (Figs. 1 and 2). The other three were situated in the middle of the delta above the POM unit. We aimed to have a pair of crossing survey lines at each site to resolve any three-dimensional (3D) effects. Line lengths were chosen to be ~1 km, long enough to determine the anticipated depths to the sediment–basement interface using seismic refraction tomography. The selection of sites and timing and execution of the field campaigns were influenced by (i) the limited availability of sufficient dry land, (ii) the timing of the flood waters, and (iii) logistical challenges associated with moving about and working within the delta given the free-ranging dangerous animals and lack of roads.

Our HR2 site (Fig. 1c) was easily accessible by land vehicles, thinly vegetated, covered by a mixture of sand and clay, and damp at the time of surveying. The Jao site near the village of Jao on the small L-shaped Jedibe Island within the upper delta was only reachable by boat or helicopter (Fig. 1b). It was largely free of trees and covered by a mixture of sand and clay with extensive patches of salt, typical of numerous small islands within the delta. The Wheat Fields and Golf Course sites, named for their surface morphology by local safari lodge operators, were located further downstream on Chief's Island (Fig. 1d and e), which at approximately 70 × 10 km is the largest area of dry land in the middle of the delta. These latter two field sites are seasonal floodplains that were dry, covered with short to medium-height grass and sand, and accessible by land vehicles at the time of surveying. The presence of animals necessitated deployment and retrieval of the cables and equipment on a daily basis at each site, thus significantly reducing the time available for making measurements.

5. Methods employed in the ground-based surveys

Our ground-based geophysical surveys were designed to provide details on the distribution of electrical resistivities (ERT and TEM methods) and the P-wave velocity structure (high resolution seismic reflection/refraction tomographic methods) beneath key parts of the delta. We employed the ERT and TEM methods in an attempt to compensate for the well-known limitations of each method (Gomez-Trevino and Edwards, 1983; Raiche et al., 1985; Harinarayana, 1999). In particular, inherently non-unique features of models derived from ERT data may be well defined in models based on TEM data, and vice-versa. Moreover, ERT models typically contain the most detailed resistivity information for shallow regions of the earth, whereas induction-based (e.g., TEM) models are usually the only ones that contain resistivity information for deep regions. Seismic reflection sections provide the highest resolution structural images throughout the depth range of interest, and seismic refraction tomograms are the most reliable source for details on P-wave velocities.

Brief information on the applications of the three ground-based geophysical methods at the four field sites is summarized below and in Table 1. Additional details on applications of the ERT and TEM methods are provided by Meier et al. (2014) and on the seismic reflection/refraction tomographic techniques by Reiser et al. (2014).

5.1. ERT

The same ERT instrumentation and recording configuration were used at all sites (Table 1). These consisted of a multichannel Syscal Pro instrument with 96 current and potential electrodes equally spaced at 5 m intervals. Six current electrode groups spaced at 50 m intervals were added to both ends of each line to provide greater depth penetration. Electrodes needed to be hammered into the ground and/or watered to reduce contact resistances at many locations. Considerable coupling problems precluded ERT measurements from being made along line 2 at HR2. Each ERT data set comprised 3550 gradient and 1974 dipole–dipole measurements using the 96 inner electrodes and 354 gradient measurements using the 12 offset electrodes.

ERT data were eliminated from the processing and inversion schemes if reciprocal measurements did not match to within 5% or if apparent resistivities were implausibly low (i.e., <1 Ω m) or implausibly high (i.e., >5000 Ω m) given the resistivities of the surface soils and sediments. In addition, inspection of pseudo-sections and the results of a series of provisional inversions allowed outlier values due to faulty channels or bad coupling to be identified and removed.

The RES2DINV code (Loke and Barker, 1996) was used to invert the ERT data. The inversion process was initiated using a homogeneous model based on the average apparent resistivity of each data set. Depth of investigation (DOI; Oldenburg and Li, 1999) estimates were calculated using start models with 0.1 and 10 times the resistivity of the original start models. Only those parts of the resistivity models with DOI values < 0.2 were considered in the interpretations.

5.2. TEM

Three different instruments were used for the TEM measurements (Table 1): Geonics Protem 47 and 57 and the WalkTEM developed at Aarhus University (Nyboe et al., 2010). The Protem 47 (used at Wheat Fields and Golf Course) has a lower moment transmitter and earlier time gates than the Protem 57 (used only at Golf Course). Consequently, the former provides better near-surface resolution and the latter supplies information at greater depths. The WalkTEM instrument (used at HR2 and Jao) has both low- and high-moment capabilities.

The TEM data were stacked, and early time gates affected by oversaturation and late time gates with unacceptably low signal-to-noise ratios were discarded. As for the regional HTEM data, Auken and Christiansen's (2004) pseudo-2D scheme was used to invert the TEM

Table 1
Ground-based survey instruments and parameters. At three sites, the TEM data were collected using both low-moment sources (numbers without brackets) and high-moment sources (numbers in brackets).

Site	HR2		Jao		Wheat Fields		Golf Course	
Line	1	2	3	4	5	6	7	8
ERT								
Lengths (m)	480	n/a	480	480	480	480	480	480
Electrode spacings (m)	5	n/a	5		5		5	
TEM								
Instruments	WalkTEM		WalkTEM		Protem 47		Protem 47/57	
# soundings	1	5	8	10	4	4	11	4
	(5)	(0)	(3)	(3)			(4)	(1)
Tx sizes (m)	40 × 40		40 × 40		100 × 100		100 × 100	
	(100 × 100)		(100 × 100)				(200 × 200)	
Time gates (μs)	11.0–8841		6.4–7125		11.9–3378		11.9–4302	
	(11.0–8841)		(6.4–7125)				(157.1–26,630)	
Moments (Am²)	1600–12,800		1600–12,800		10,000–3300		10,000–35,000	
	(10,000–80,000)		(10,000–80,000)				(320,000–800,000)	
Seismic								
Lengths (m)	1345	960	1410	1180	1070	830	1920	1340
Geophone spacings (m)	4		5		5		4	
Source spacings (m)	8		10		10		8	
Energy sources	Pipegun with 12-gauge blank cartridges		Pipegun with 12-gauge blank cartridges		Pipegun with 12-gauge blank cartridges		Mechanical hammer 6–8 stacks per source location	

data. We tested a range of start models for the inversions of each data set. Start models based on the nearest HTEM models generally produced the quickest convergences and most satisfactory models in terms of the root-mean-square (RMS) differences between observed and model-predicted data. Models with either 3- or 4-layers plus a half-space were necessary to explain the data. A standard deviation factor (STDF) was derived for all layer resistivities and depths using the diagonal elements of the linearized posterior model covariance matrix (Auken et al., 2005). An STDF value of 1.0 signifies an error-free parameter, whereas an STDF of 1.1 indicates that a parameter has an error of about 10%. Auken et al. (2005) consider model parameters to be well determined if STDF values are <1.2, reasonably well-determined if they are 1.2 to <1.5, poorly determined if they are 1.5 to 2, and largely undetermined if they are >2.

5.3. Seismic reflection processing and refraction tomographic inversions

All seismic data were collected using Geometrics Geodes with 192 channels and single 30 Hz geophones spaced at 4 or 5 m intervals (Table 1). A pipegun that detonated blank shotgun cartridges at nominal 1 m depths every 8 or 10 m along the lines was used as the seismic source at HR2, Jao, and Wheat Fields. Because of temporary difficulties involved with transporting shotgun cartridges, we used a 40 kg mechanically driven hammer that struck a metal plate for the source at Golf Course. In addition to the seismic sources within the recording lines, multiple pipegun shots or hammer blows offset by up to 200 m from the ends of the lines were used to generate deeper travelling waves.

Initial processing included geometry assignment and editing of the data. First-arrival times were then picked, generally to an accuracy of 2–8 ms depending on the proximity of the receivers to the sources and local noise conditions. These first-arrival times were inverted using a 2D refraction tomographic scheme (Lanz et al., 1998; Reiser et al., 2014) with laterally homogeneous starting models derived from 1D velocity-depth inversions of the same first-arrival times.

A standard suite of seismic reflection processing steps (Reiser et al., 2014) applied to each line of data yielded seismic time sections. These steps included amplitude scaling, time-variant spectral whitening, refraction and residual static corrections, stacking velocity analyses, NMO corrections, and CMP stacking. Since all significant reflection horizons were subhorizontal and no significant diffractions were recorded, the sections were not migrated. The seismic time sections were converted to depth images using the tomographic P-wave velocities; similar depth images were obtained using interval velocities derived from the stacking velocities.

6. Results

Processing and inversion results for the HR2 data sets are presented in Figs. 3–5, for the Jao data sets in Figs. 6–8, for the Wheat Fields data sets in Figs. 9–11, and for the Golf Course data sets in Figs. 12–14. Because all models are essentially 1D in nature below ~20 m depth, the horizontally averaged ERT, TEM, and HTEM resistivity models in Figs. 5, 8, 11, and 14 highlight many of the similarities and differences in the details provided by the three approaches.

Most of the model parameters (i.e., depths, thicknesses, resistivities, and velocities) cited in the following text are approximations of the average values shown in the various figures. We refer to elements with resistivities greater than ~100 Ω m as highly resistive or resistive and elements with resistivities less than ~20 Ω m as conductive. Elements with resistivities between these values are referred to as moderately resistive. Elements with resistivities greater than 1000 Ω m are referred to as very resistive. P-wave seismic velocities of <1000, ~1800, and ≥4500 m/s are referred to as very low, low, and high, respectively.

6.1. Common features

Despite the 1075-m-long acquisition lines, the ERT models provide dependable resistivity information to depths of only 40–60 m (Figs. 3a, 6a and e, 9a and e, and 12a and e). The shallow maximum depths at HR2, Wheat Fields, and Golf Course are consequences of limited current penetration through the thin resistive surface layer of dry sand and significant current channelling in the conductive underlying layer. At Jao, the shallow maximum depths are probably the result of current channelling within the thick near-surface conductive layer of saline-water saturated sand and clay. As expected, the ERT models contain the highest resolution resistivity information for the upper 20–40 m at each site. Based on the results of studies involving synthetic and field ERT and TEM data (e.g., Gomez-Trevino and Edwards, 1983; Raiche et al., 1985; Spies and Frischknecht, 1991), the ERT-based resistivities are likely to be our most reliable estimates for this depth range. The distinct gradients in the lower 20 m of all ERT models (Figs. 5, 8, 11, and 14) could represent transition zones or they could be artefacts
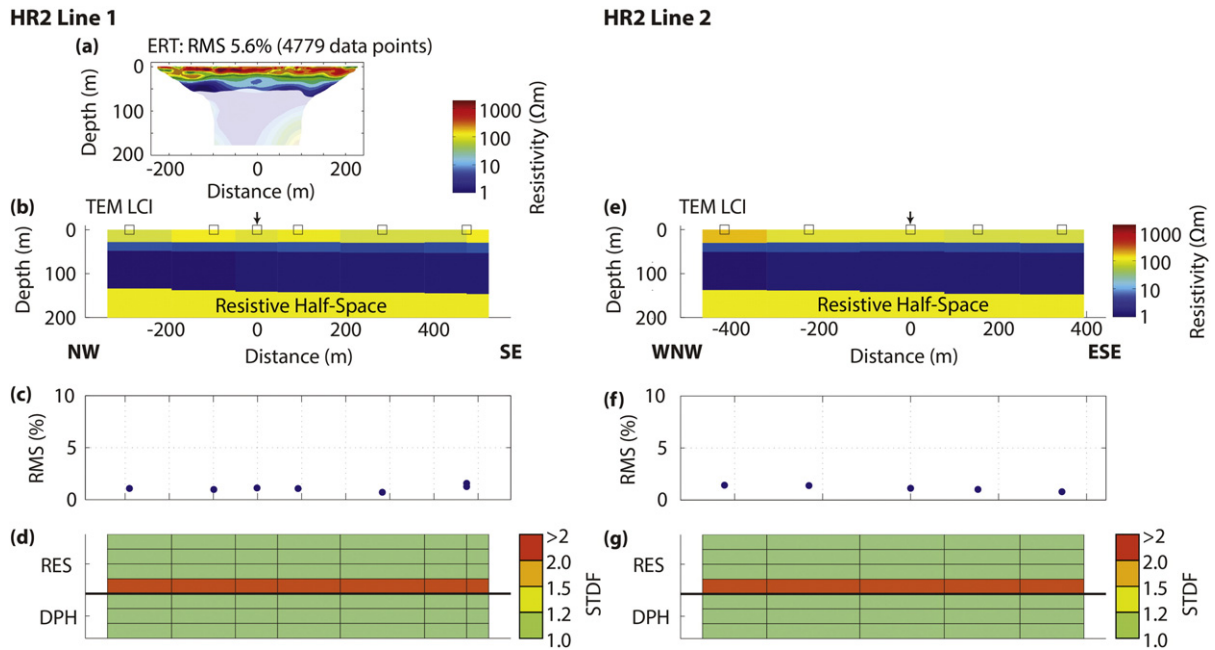
Fig. 3. Inversion results for ERT and TEM data acquired at the HR2 site. (a) Line 1 resistivity model derived from a smoothness-constrained inversion of the ERT data with semi-opaque overlay covering regions with depth of investigation (DOI) values > 0.2. (b) Line 1 resistivity model derived from a laterally constrained inversion of the TEM data. (c) Line 1 RMS differences between observed and model-predicted TEM data. (d) Line 1 standard deviation factors (STDF) for resistivities (RES; top four rows) and depths (DPH; bottom three rows) of model layers 1–4 displayed in (b). (e)–(g) Same as (b) to (d) but for line 2 TEM data. Arrows in (b) and (e) identify the intersection point of the two lines.

associated with the regularization used to constrain the inversions (Meier et al., 2014). RMS misfits are 4.4–6.9% for the ERT observed and model-predicted data.

The TEM and HTEM models contain the same principal features at each site (i.e., an overall resistive–conductive–resistive structure at HR2, Wheat Fields, and Golf Course, and an overall conductive–resistive structure at Jao), with similar estimates for the resistivities and depths to the upper and lower boundaries of the intermediate-depth conductive layer (Figs. 5, 8, 11, and 14). Resistivity estimates of the moderately to highly resistive layers are similar for some of the TEM and HTEM models and different for others.

RMS misfits are 1.0–5.0% for the TEM observed and model-predicted data. STDF values indicate that the resistivities and interface depths of the conductive layer are well determined in all TEM models, but that resistivities of the moderately to highly resistive layers range from largely undetermined to well determined (Figs. 3, 6, 9, and 12). As examples,

the resistivities of the shallow moderately to highly resistive layer are well determined in the HR2, Wheat Fields, and Golf Course TEM models, but the resistivities of the resistive half-space are poorly to largely undetermined in all models. These results are consistent with those of previous synthetic and field studies (Mallick and Verma, 1979; Gomez-Trevino and Edwards, 1983; Raiche et al., 1985), which have demonstrated that inversions of high quality TEM data yield reliable model parameters for large conductors and variably reliable resistive-unit resistivities.

Like the ground-based TEM models, resistivities of the resistive half-space in the HTEM models range from poorly to largely undetermined (Meier et al., 2014). Since the early recordings in transient electromagnetic techniques provide information for estimating the resistivities and thicknesses of shallow layers, there is an additional inherent limitation of our HTEM models. Contamination by residual source currents required that a large proportion of recordings made before 113 μs be
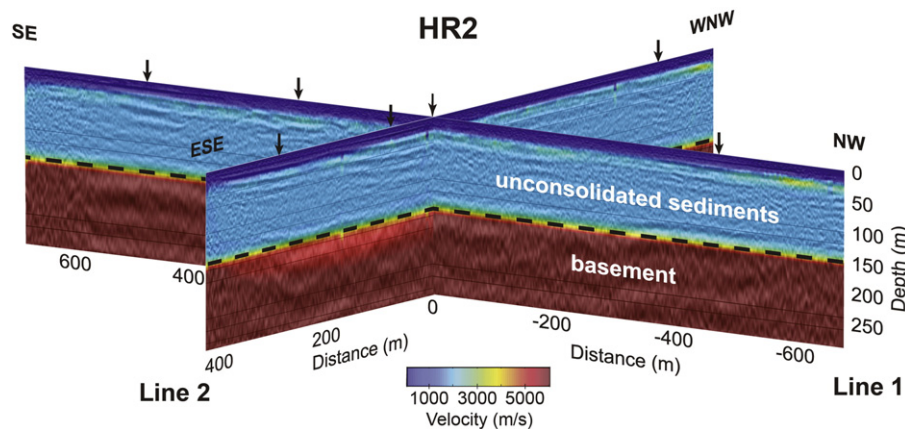

Fig. 4. Reflection images and superimposed refraction tomographic velocities (colours) derived from high resolution seismic data acquired along lines 1 and 2 at the HR2 site. Dashed line identifies the interpreted boundary between sediments and basement. Arrows identify images of buried river valleys. Origin of distance scale is same as for ERT and TEM models. RMS differences between model-predicted and observed first arrival times are (line 1) 6.6 ms and (line 2) 5.6 ms.
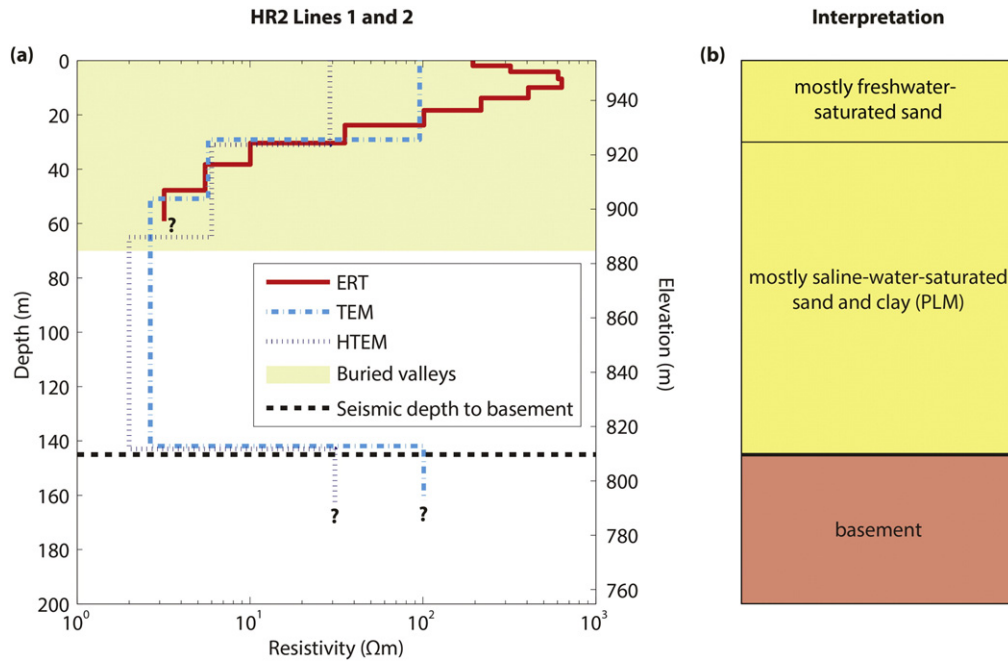
Fig. 5. HR2 models and interpretation. (a) Horizontally averaged ERT, TEM, and HTEM resistivity models and seismic basement depth. Shading: region of curvilinear and irregular reflectors. (b) Corresponding hydrogeological interpretation. Yellow: sediments. Pink: basement.

excluded from the inversion process (Podgorski et al., 2013a). By comparison, only recordings before 11–27 μs were excluded from inversions of the TEM data. Our inversion tests have demonstrated that the lack of early recordings significantly affected HTEM model parameter estimates for the uppermost layer. Because the average HTEM model resistivities of this layer are unlikely to be trustworthy, they are not discussed further in this contribution.

Coloured representations of the tomographic P-wave velocities are superimposed on the seismic reflector images in Figs. 4, 7, 10, and 13. Observed and model-predicted traveltimes have RMS misfits of 3.3–7.4 ms. The tomograms for all sites are characterized by three seismic layers with velocities that are very low, low, and high. Depths

to the boundaries between the layers are nearly constant at each site but vary from site to site. The sediment–basement interfaces identified on the seismic images are primarily based on coincident abrupt transitions from low to high velocities and prominent subhorizontal reflectors. Basement depths are estimated to have accuracies in the ± 10 m range based on the seismic velocities and periods of the interface reflections.

6.2. HR2 site

The upper 30 m of the ERT resistivity model for HR2 line 1 (Fig. 3a) is a heterogeneous layer that has moderate to high resistivities
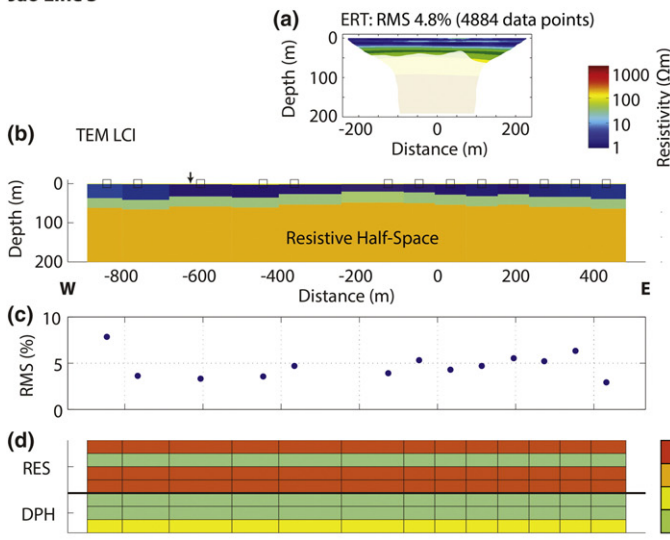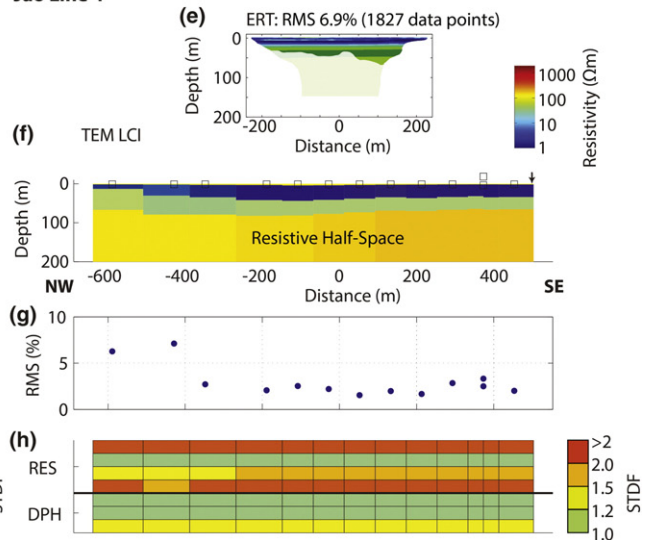

Fig. 6. Inversion results for ERT and TEM data acquired at the Jao site. (a) Line 3 resistivity model derived from a smoothness-constrained inversion of the ERT data with semi-opaque overlay covering regions with DOI values > 0.2. (b) Line 3 resistivity model derived from a laterally constrained inversion of the TEM data. (c) Line 3 RMS differences between observed and model-predicted TEM data. (d) Line 3 standard deviation factors (STDF) for resistivities (RES; top four rows) and depths (DPH; bottom three rows) of model layers 1–4 displayed in (b). (e)–(h) Same as (a) to (d) but for line 4 ERT and TEM data. Arrows in (b) and (f) identify the intersection point of the two lines.
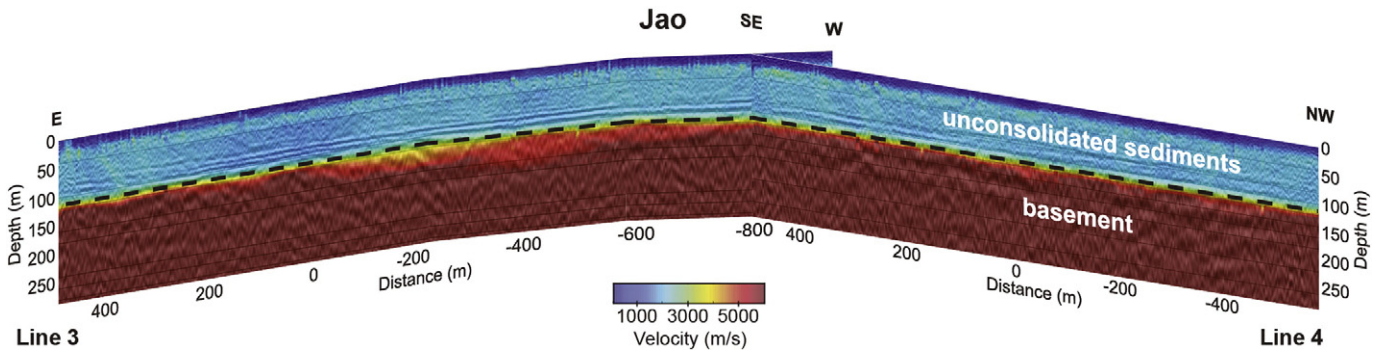
Fig. 7. Reflection images and superimposed refraction tomographic velocities (colours) derived from high resolution seismic data acquired along lines 3 and 4 at the Jao site. Dashed line identifies the interpreted boundary between sediments and basement. Origin of distance scale is same as for ERT and TEM models. RMS differences between model-predicted and observed first arrival times are (line 3) 4.0 ms and (line 4) 4.7 ms.

(50–1000 Ω m with most values in the 300–400 Ω m range). Although this layer is clearly underlain by a conductive feature (represented by the resistivity gradient extending to 60 m depth in Fig. 5a), the resistivity and depth of this feature are not well determined in the ERT model. Resistivity models derived from the TEM data recorded along lines 1 and 2 also include an upper 30-m-thick resistive layer underlain by conductive material (Fig. 3b and e). These models do not resolve the shallow heterogeneity observed in the ERT model, but they suggest that the conductive material extends from 30 to 142 m depth, below which the resistivity markedly increases within the half-space. STDF values (Fig. 3d and g) indicate that all layer resistivities and depths are well resolved except for the resistivity of the half-space.

Interfaces between the three layers in the velocity tomograms are at 20 and 145 m depths (Fig. 4). In addition to the subhorizontal basement reflector at 145 m depth, there are several curvilinear and irregular reflectors in the upper 70 m of the HR2 seismic images.

Resistivities in the ERT, TEM, and HTEM models are similar from 30–60 m depth and resistivities in the TEM and HTEM models are practically the same from 60 m depth to the top of the resistive half-space,

which coincides with the seismically determined basement depth (Fig. 5a).

6.3. Jao site

The absence of a thick near-surface layer with moderate to high resistivities distinguishes Jao from the other three field sites. ERT models for lines 3 and 4 (Fig. 6a and e) include a thin heterogeneous layer of variable resistivity (8–250 Ω m; not observable at the scale of the diagrams in Fig. 6, but seen in the average values in Fig. 8a) from the surface to 2 m depth that overlies a conductive (1–22 Ω m) layer that extends to 32 m depth. Models derived from the TEM data (Fig. 6b and f) contain a poorly resolved thin layer with high resistivities (100 Ω m; again, not observable at the scale of the diagrams in Fig. 6, but seen in the average values in Fig. 8a) to 2 m depth. This is underlain successively by a conductive (3 Ω m) layer from 2–35 m, a moderately resistive (~50 Ω m) layer from 35–65 m, and a resistive (200 Ω m) half-space below 65 m. STD factors (Fig. 6d and h) indicate that only the resistivity and depths to the top and bottom of the conductive layer are well resolved in the TEM models.
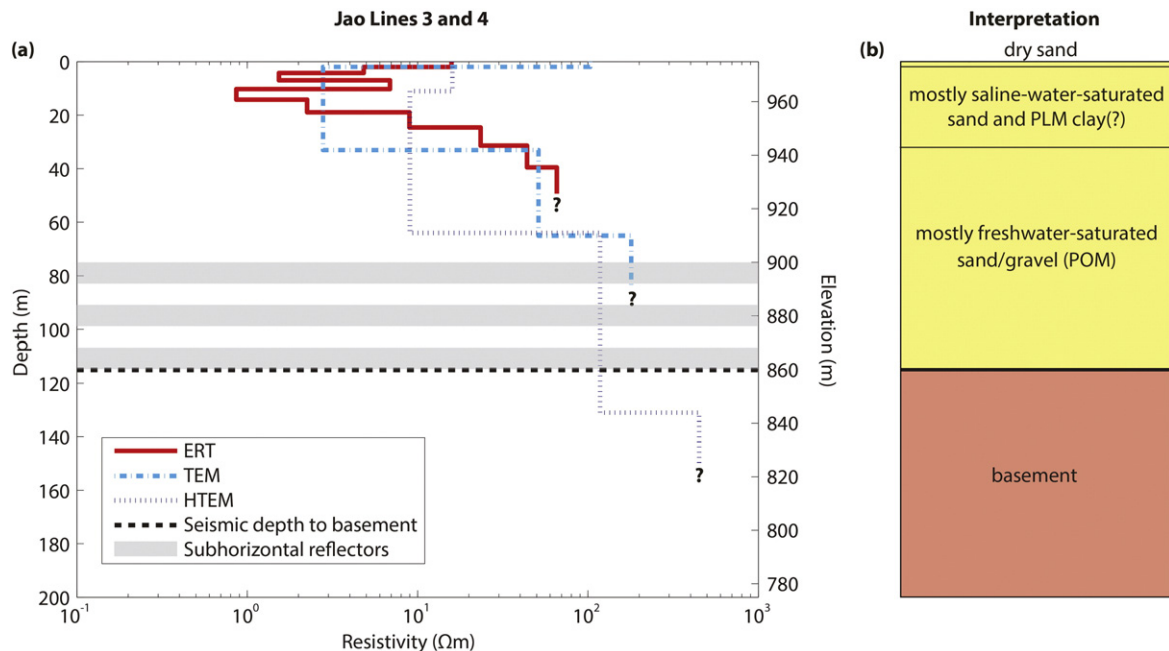

Fig. 8. Jao models and interpretation. (a) Horizontally averaged ERT, TEM, and HTEM resistivity models, location of continuous subhorizontal reflectors, and seismic basement depth. (b) Corresponding hydrogeological interpretation. Yellow: sediments. Pink: basement.
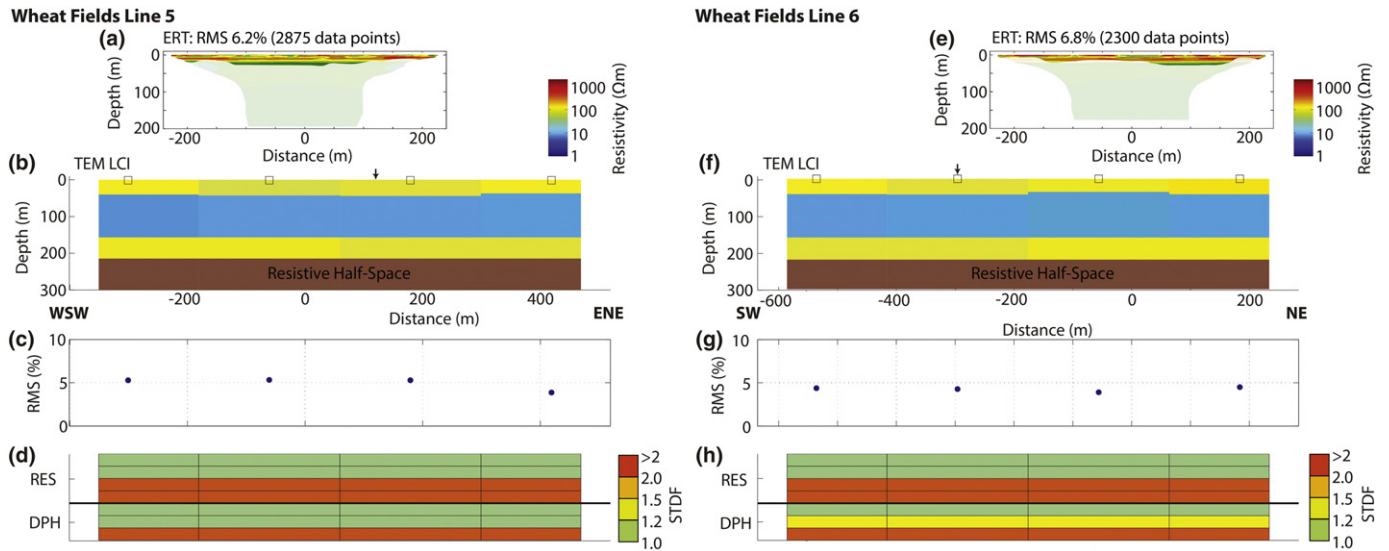
Fig. 9. Inversion results for ERT and TEM data acquired at the Wheat Fields site. (a) Line 5 resistivity model derived from a smoothness-constrained inversion of the ERT data with semi-opaque overlay covering regions with DOI values > 0.2. (b) Line 5 resistivity model derived from a laterally constrained inversion of the TEM data. (c) Line 5 RMS differences between observed and model-predicted TEM data. (d) Line 5 standard deviation factors (STDF) for resistivities (RES; top four rows) and depths (DPH; bottom three rows) of model layers 1–4 displayed in (b). (e)–(h) Same as (a) to (d) but for line 6 ERT and TEM data. Arrows in (b) and (f) identify the intersection point of the two lines.

P-wave velocity transitions beneath Jao are observed at 10 and 115 m depths (Fig. 7). There are strong continuous subhorizontal reflectors in the 75–115 m depth range, the lower one of which is the sediment–basement boundary.

Trends of resistivities in the upper 50 m are generally consistent in the ERT and TEM models at Jao (Fig. 8a). Both the TEM and HTEM models contain a resistivity increase at 65 m depth. The HTEM model also includes a resistivity increase at 130 m depth, 15 m below the seismically determined basement depth.

6.4. Wheat Fields site

ERT models for lines 5 and 6 reveal moderate to high resistivities (65–500 Ω m) in the top 20 m of the Wheat Fields site (Fig. 9a and e). In the TEM models (Fig. 9b and f), a relatively homogeneous version of this layer extends to 40 m depth with a lower average resistivity

(100 Ω m). It is underlain successively by a conductive (17 Ω m) layer from 40 to 160 m, a noticeably more resistive (100 Ω m) unit from 160 to 220 m, and a highly resistive (>1000 Ω m) half-space below 220 m. STDF values (Fig. 9d and h) indicate that the TEM models are generally well determined except for the depth to the half-space and the resistivities of the bottom layer and half-space.

Velocity increases in the Wheat Fields seismic tomograms occur at depths of 10 and 207 m (Fig. 10). The top 60 m of the seismic images contain no significant reflectors. Semi-continuous subhorizontal reflectors are observed at 65–90 m depth and variably strong continuous subhorizontal reflectors are observed at 130–207 m. The lowermost reflector is the top of basement.

Resistivities in the top 20 m at Wheat Fields are well resolved in the ERT models and those from 40–160 m depth are relatively well defined in the TEM and HTEM models (Fig. 11a). We are not confident of any resistivity estimate for the 20–40 m depth range. ERT resistivity estimates
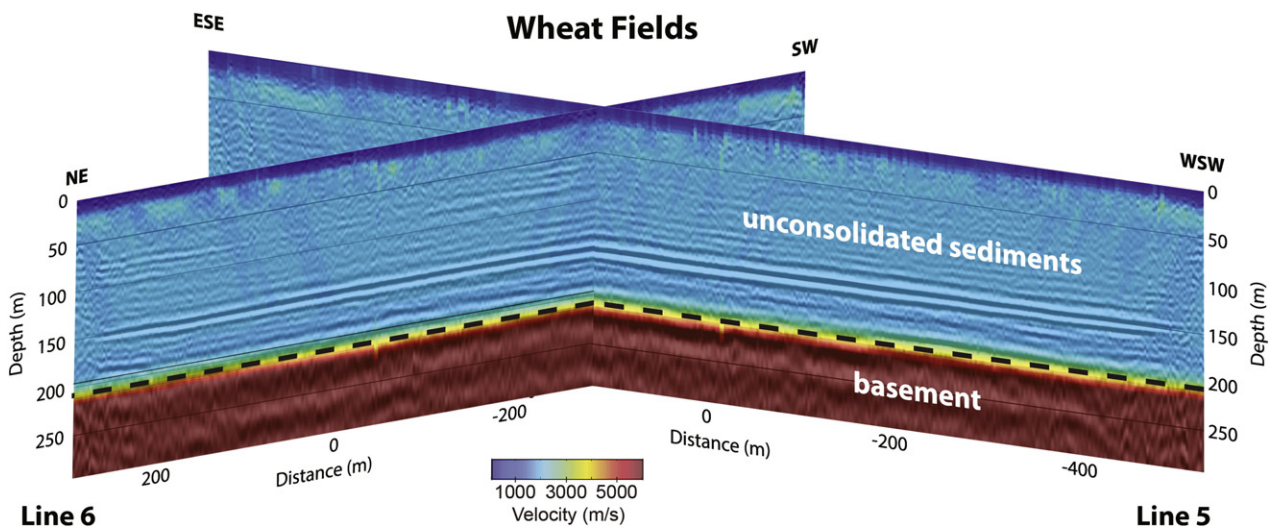

Fig. 10. Reflection images and superimposed refraction tomographic velocities (colours) derived from high resolution seismic data acquired along lines 5 and 6 at the Wheat Fields site. Dashed line identifies the interpreted boundary between sediments and basement. Origin of distance scale is same as for ERT and TEM models. RMS differences between model-predicted and observed first arrival times are (line 5) 3.3 ms and (line 6) 3.5 ms.
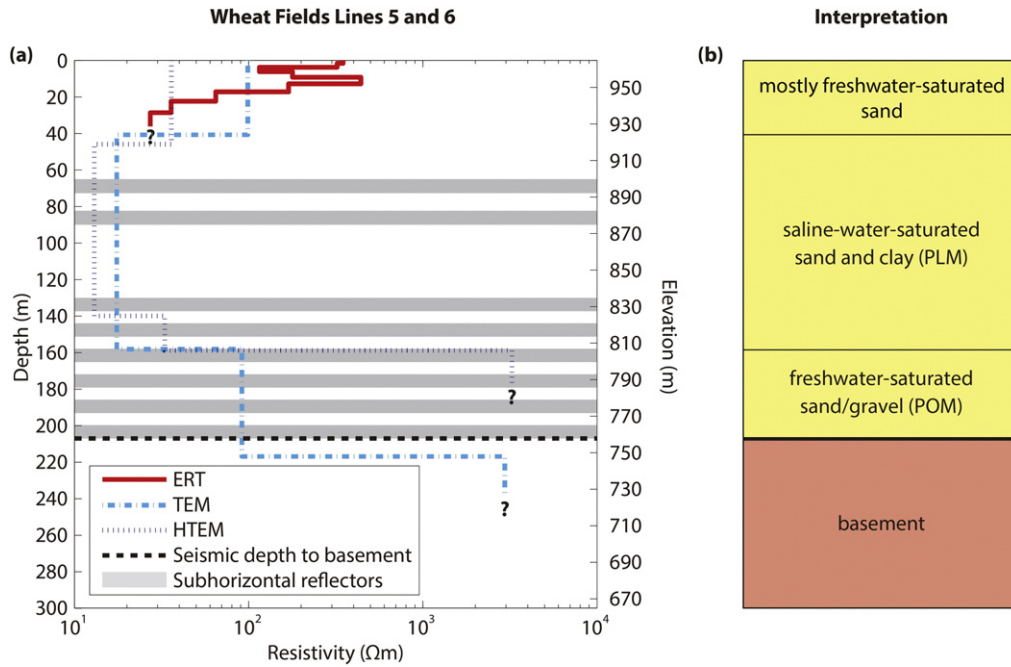
Fig. 11. Wheat Fields models and interpretation. (a) Horizontally averaged ERT, TEM, and HTEM resistivity models, location of continuous subhorizontal reflectors, and seismic basement depth. (b) Corresponding hydrogeological interpretation. Yellow: sediments. Pink: basement.

at this level may be affected by limited current penetration, and, for our TEM instrumental setup, resolution of resistivity variations in the TEM models is comparatively low in this depth range. The top of the highly resistive half-space in the TEM models practically coincides with the seismically determined basement depth.

6.5. Golf Course site

Inversions of the ERT data acquired along lines 7 and 8 at Golf Fields yield models (Fig. 12a and e) with high resistivities (250–400 Ω m) that extend from the surface to 25 m depth, below which resistivities steadily

decline. The TEM models (Fig. 12b and f) also contain a 25-m-thick surface layer of high resistivities (>200 Ω m). This is successively underlain by a moderately resistive (55 Ω m) layer from 25–56 m, a conductive (17 Ω m) layer from 56–190 m, a moderately resistive (65 Ω m) unit from 190–235 m, and a highly resistive (1500 Ω m) half-space below 235 m. The STD factors indicate that all model parameters are well resolved except for the resistivities of the lower layer and half-space. Note, that resistivities in the lower layer along the entire length of line 7 are reasonably well determined. Although numerical estimates of resistivity in deeper parts of the models are poorly defined, increases in apparent resistivities in the late time gates (e.g., Fig. 15, which is
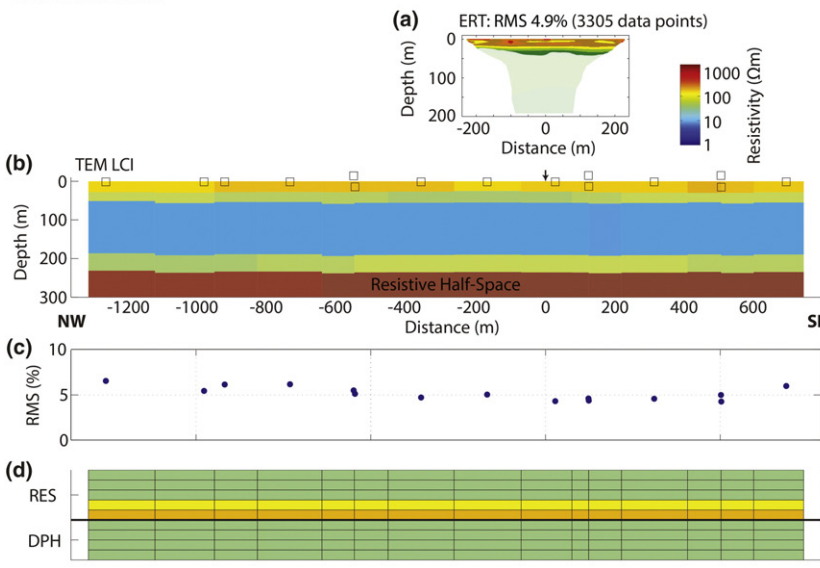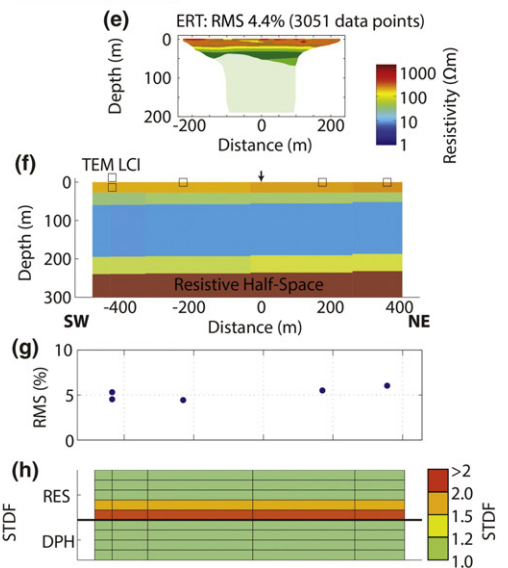

Fig. 12. Inversion results for ERT and TEM data acquired at the Golf Course site. a) Line 7 resistivity model derived from a smoothness-constrained inversion of the ERT data with semi-opaque overlay covering regions with DOI values > 0.2. (b) Line 7 resistivity model derived from a laterally constrained inversion of the TEM data. (c) Line 7 RMS differences between observed and model-predicted TEM data. (d) Line 7 standard deviation factors (STDF) for resistivities (RES; top four rows) and depths (DPH; bottom three rows) of model layers 1–5 displayed in (b). (e)–(h) Same as (a) to (d) but for line 8 ERT and TEM data. Arrows in (b) and (f) identify the intersection point of the two lines.
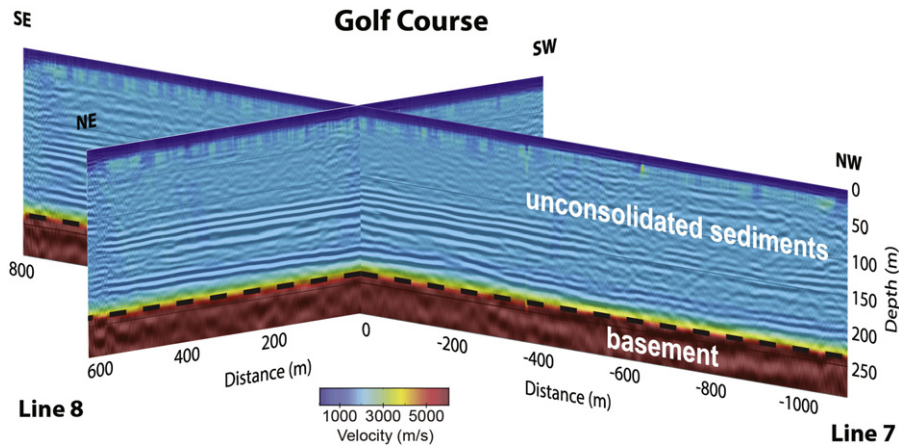
Fig. 13. Reflection images and superimposed refraction tomographic velocities (colours) derived from high resolution seismic data acquired along lines 7 and 8 at the Golf Course site. Dashed line identifies the interpreted boundary between sediments and basement. Origin of distance scale is same as for ERT and TEM models. RMS differences between model-predicted and observed first arrival times are (line 7) 7.4 ms and (line 8) 5.9 ms.

representative of the combined Protem 47 and 57 data recorded at the Golf Course site) require significant increases in resistivity at these depths.

The two increases in seismic velocity are observed at depths of 15 and 235 m at the Golf Course site (Fig. 13). Conspicuous subhorizontal reflectors are imaged in the 122–235 m depth range. Again, the top-of-basement reflector is the deepest continuous feature.

Fig. 14a demonstrates the good correspondence between the upper 50 m of the ERT and TEM models. The resistivities and upper and lower boundaries of the conductive layer are practically identical in the TEM and HTEM models. The lowermost boundary of the TEM model coincides with the top of the seismically defined basement.

7. Discussion

To understand the significance of the geophysical models, it is necessary to consider the physical properties of sediments and basement

rocks interpreted to underlie the delta. Resistivities of sediments are known to be strongly dependent on the saturation conditions, the salinity of the pore fluids, and the clay content (Archie, 1942; Knight and Endres, 2005), such that the dry and freshwater-saturated sand at the surface and shallow subsurface throughout much of the delta is likely to be moderately to highly resistive and the saline-water-saturated sand and clay observed on some islands and encountered in boreholes are likely to be conductive. Basement rocks underlying the sediments are expected to be highly resistive. Very low velocities and low velocities in the refraction tomograms are diagnostic of dry and water-saturated sediments (Stümpel et al., 1984; Büker et al., 1998), respectively, whereas the high velocities are typical of Precambrian and Karoo basement rocks (Bräuer et al., 2007; Schmelzbach et al., 2008).

We first discuss our integrated interpretations of the resistivity and P-wave velocity models for each site and then evaluate the seismic reflection images. Finally, the impact of the new information and
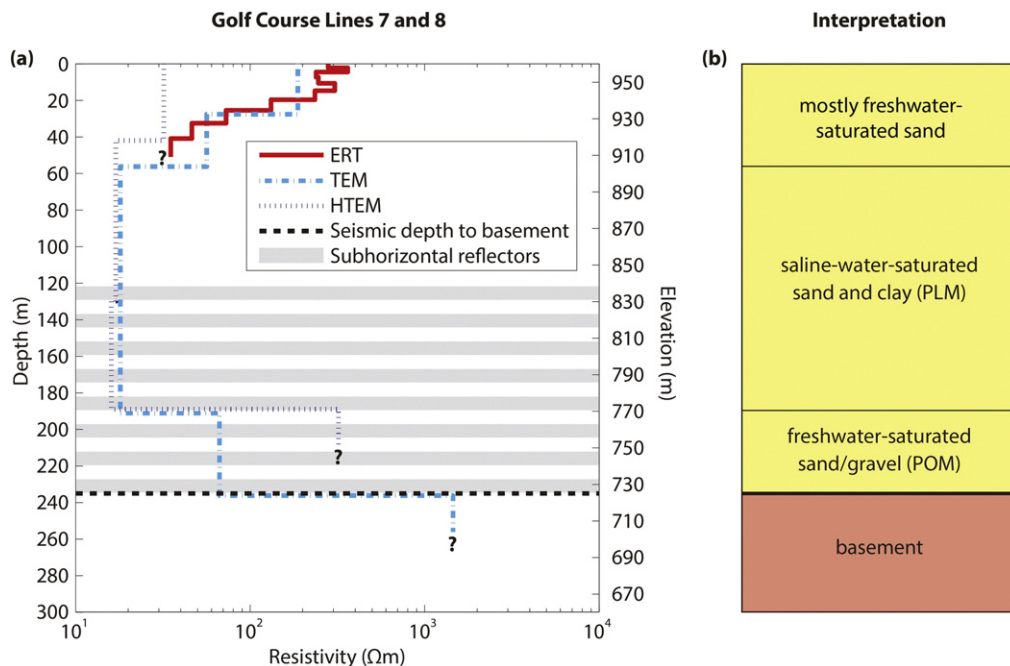

Fig. 14. Golf Course models and interpretation. (a) Horizontally averaged ERT, TEM, and HTEM resistivity models, location of continuous subhorizontal reflectors, and seismic basement depth. (b) Corresponding hydrogeological interpretation. Yellow: sediments. Pink: basement.
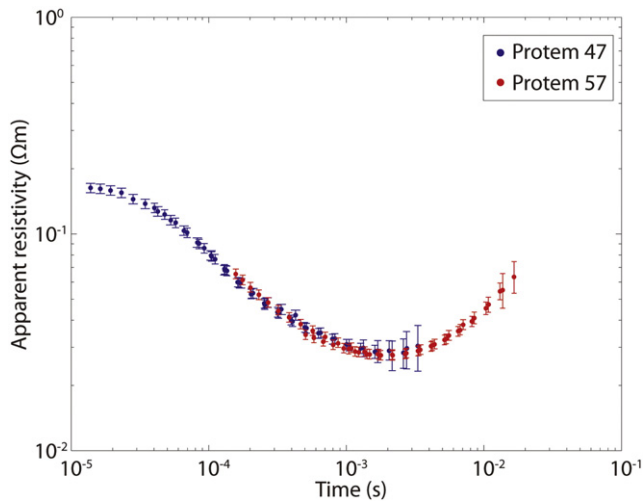
Fig. 15. Typical apparent resistivity curves for TEM data acquired at a single location along Golf Course line 7 using the low-moment Geonics Protem 47 instrument (blue dots with standard deviations) and the high-moment Geonics Protem 57 instrument (red dots with standard deviations). For each instrument, the data were acquired using three repetition rates with three different suites of time gates. Although apparent resistivities in the late time gates of the Protem 47 data only suggest the existence of higher resistivities at greater depths, the increasing apparent resistivities in the late time gates of the Protem 57 data unambiguously require the presence of higher resistivities at these depths.

interpretations on Podgorski et al.'s (2013b) proposed four-unit geological/hydrogeological model of the Okavango Delta region is assessed.

7.1. HR2 site

Of the four field sites, the HR2 models are the most straightforward to interpret (Fig. 16). All HR2 resistivity models (Figs. 3 and 5) include a

30-m-thick layer of moderate to high resistivity overlying a conductive layer and a resistive half-space. The conductive layer continues to 142–144 m depth in the TEM and HTEM models. According to the seismic refraction tomograms, P-wave velocities are very low in the upper few meters and uniformly low to depths of 145 ± 10 m beneath HR2. Combining these observations with the physical property information, we reason that the upper moderately to highly resistive layer comprises unsaturated surface sand overlying freshwater-saturated sand and that the conductive layer is composed of saline-water-saturated sand and clay (Fig. 5b).

Our seismically defined basement depth of 145 ± 10 m is similar to basement depths of 135 and 150 m estimated from vintage seismic refraction data acquired 9 km to the north and 14 km to the northeast of HR2, respectively (Greenwood and Carruthers, 1973), and to a 129 m basement depth observed in a borehole 14 km to the northwest (T. Preston, personal communication, 2010). These values are consistent with the expected regional attitude of the basement, with increasing depths towards the centre of the delta and towards the main southeastern fault of the half-graben. Based on the near coincident depths in the resistivity and seismic models, there is little doubt that the top of the resistive half-space corresponds to the upper surface of the basement beneath HR2 (Fig. 5).

7.2. Jao site

Jao is unique among the four sites in that it is on a small island surrounded by channels and perennial flood plains, whereas the others lie within dry open expanses of land. There are several consequences related to Jao's location on a small island: (i) like many small islands within the delta, the near-surface layer on Jedibe Island partly comprises conductive saline-water-saturated sand, whereby the salt deposits were created by intense evapotranspiration; (ii) because of its large footprint, the HTEM system continuously sampled both the island and adjacent regions covered by resistive fresh water as it crossed the narrow width of the island (Meier et al., 2014); (iii) it is likely that the TEM data, which were recorded along the edges of the island (Fig. 1b),
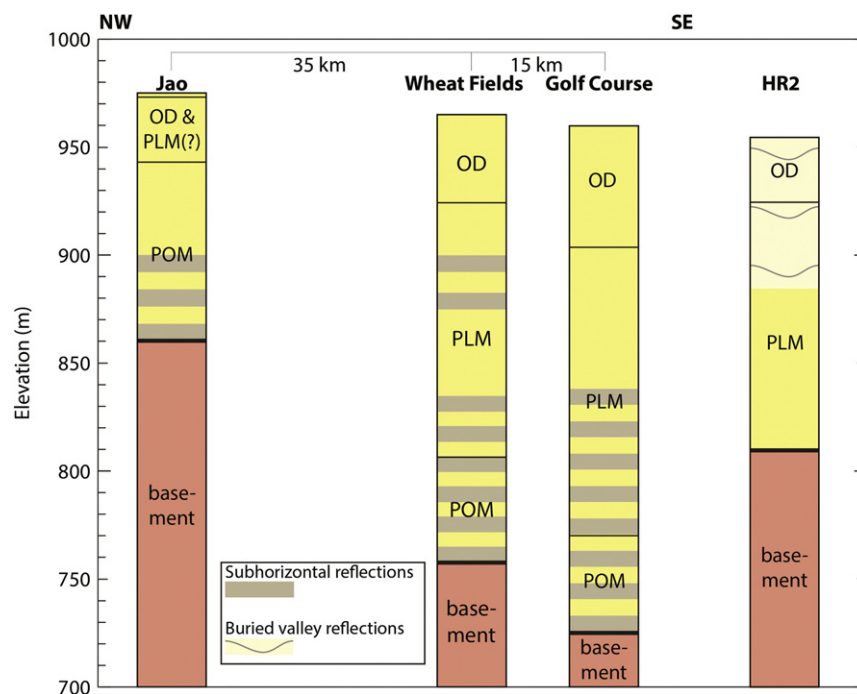

Fig. 16. Compilation of models for all study sites (e.g., Figs. 5b, 8b, 11b, and 14b) aligned according to elevation. The Jao, Wheat Fields, and Golf Course models are approximately positioned by NW–SE distance (general direction of inclination of the delta). The HR2 section is not aligned with the other sites. Yellow: sediments. Pink: basement. Broad horizontal stripes: subhorizontal reflectors. Curves and light yellow in HR2 column: region of curvilinear and irregular reflectors.

were also affected by resistivity and hydrogeological differences between the island and adjacent wetlands. In addition to possible differences in salinity deep beneath the island and adjacent wetlands (see discussions in Milzow et al., 2009 and references therein), 3D lateral heterogeneity associated with the top few metres of land and open fresh water may have affected the TEM and HTEM models at all depth levels.

Despite the above-mentioned complications, the various resistivity models appear to provide limited useful information. The high resistivities (Fig. 6) and very low P-wave velocities (Fig. 7) of the poorly defined thin layer at the surface are indicative of dry material (Fig. 8b). Low P-wave velocities demonstrate that sediments extend to 115 ± 10 m depth. The conductive layer that can be traced to 32 m depth is explained by the presence of saline-water-saturated sand and clay (Fig. 8b). Distinct increases in resistivity with depth identify changing conditions. The combination of moderate to high resistivities and low P-wave velocities between 32 and 115 ± 10 m likely represents freshwater-saturated sand. High P-wave velocities are compelling evidence for basement rocks below 115 ± 10 m.

7.3. Wheat Fields and Golf Course sites

Geophysical models and their interpretation are similar for Wheat Fields and Golf Course (Figs. 11 and 14). This is not surprising given their close proximity to each other (17 km) and similar conditions on Chief's Island. Very low and low P-wave velocities demonstrate that sediments extend to depths of 207/235 m (Wheat Fields/Golf Course) beneath the two sites (Figs. 10 and 13). Resistivity estimates provide constraints on the types of sediment and the salinity of their pore waters. The upper moderately to highly resistive layers and intermediate-depth conductive layers (Figs. 9 and 12) are evidence for 40/56 m of dry and freshwater-saturated sand overlying saline-water-saturated sand and clay that extend to 160/190 m depths. Low P-wave velocities and moderate to high resistivities at depths of 160–207/190–235 m are best explained by the presence of freshwater-saturated sand.

Onset of high to very high resistivities and high P-wave velocities identify the top of basement at 220/235 m depths. Although inversions of the TEM data yield high to very high resistivities in the half-spaces (i.e. basement) of all models at both sites, the resistivity values are not well determined. However, similar very high values are required in resistivity models for the Wheat Fields site that result from jointly inverting the TEM data and deeper penetrating audiomagnetotelluric and controlled-source audiomagnetotelluric data constrained by the seismic basement depths (Kalscheuer et al., in revision).

7.4. Seismic reflection images

In addition to the abrupt P-wave velocity increase and conspicuous subhorizontal basement reflector at each site, the sediment–basement boundary at Jao, Wheat Fields, and Golf Course is distinguished by distinct changes in seismic reflector facies from prominent subhorizontal layered reflectors above to featureless and highly complex below. A change in seismic facies at the sediment–basement interface is less obvious at HR2.

The laterally continuous subhorizontal reflectors in the 75–115 m, 130–207 m and 122–235 m depth intervals at Jao, Wheat Fields, and Golf Course, respectively, are evidence for time-varying sedimentation processes and/or surface conditions. Although there are no logged boreholes in the vicinity of the geophysical field sites, key information is provided by the 90-m-deep borehole in the northeastern part of the delta (Bauer, 2004) and the numerous relatively deep (i.e., ≤180 m) boreholes to the southeast (MMEWR, 2004; Milzow et al., 2009; Podgorski et al., 2013b). The 90-m-deep borehole intersects layers of sand and a 35-m-thick layer of sandy clay, whereas the boreholes to the southeast, which have been geologically and geophysically logged, intersect multiple sand-, silt- and clay-rich layers. Thicknesses of

the layers in these latter boreholes vary from the sub-metre scale (as identified on gamma logs) through the metre scale (sampling interval of the geological logs) to tens of metres. Intercalated layers with thicknesses of 2–10 m mapped along several lines of boreholes are most relevant for our interpretation of the seismic reflection sections. Such layering beneath the geophysical field sites would explain the ~10 m depth intervals between the laterally continuous reflectors in the seismic images (Figs. 7, 10, and 13). Although the numerous relatively thin layers identified in the boreholes may be important for climatological, geological, and hydrological studies, the comparatively low frequencies of our seismic data prevent them from being imaged.

Multiple intercalated sedimentary layers that parallel the subhorizontal to gently dipping basement surface require deposition in low energy regimes, such as gently dipping delta-like environments or lakes. Some of the layers could be overbank or waning flood deposits (Miall, 1985). By comparison, the very low dip of the basement and overlying sedimentary layers likely precludes an explanation in terms of turbidites (Mandl, 1981; Prior and Coleman, 1984): the average southeasterly dip of the basement across the delta is ~0.09° (based on borehole observations at the mouth of the panhandle and seismic refraction results near Maun; see Fig. 1 in Podgorski et al., 2013b), and our seismic-determined basement depths at Jao, Wheat Fields, and Golf Course indicate average dips between these sites of 0.16° and 0.11°. The very low southeasterly dips of the basement and layering apparent at the regional scale are not resolvable on the short seismic sections.

From the character of reflectors in our seismic images alone, it is not possible to establish whether the layered sediments were deposited in a gently dipping delta-like environment or in a lake. Layered sediments that parallel a gently dipping basement floor or depositional surface have been observed in several deltas worldwide (e.g., Lake Malawi (Scholz, 1995), Lake Geneva (Baster et al., 2003), Snake River Plain (Wood, 1994)) and are ubiquitous in lakes on every continent.

In addition to the 145-m-deep subhorizontal basement reflector at HR2, there are several curvilinear (upward concave) and irregular reflectors in the upper 70 m of the two seismic images at this site (marked by arrows in Fig. 4). We interpret these reflectors as buried river channels that were active quite late in the history of the delta. During our reconnaissance survey of HR2 and adjacent areas, we observed several dry river channels at the surface; abandonment of river channels is clearly a common occurrence along the western margin of the delta (see also discussion in McCarthy, 2013).

7.5. Four-unit geological/hydrogeological model of the Okavango Delta region

Our results from the ground-based geophysical surveys support Podgorski et al.'s (2013b) proposed four-unit geological/hydrogeological model of the Okavango Delta region (Fig. 16). At increasing depths, the units are: (i) current Okavango Delta (OD), (ii) Paleo Lake Makgadikgadi (PLM), (iii) Paleo Okavango Megafan (POM), and (iv) basement. Based on the surface and borehole geological information and the helicopter and ground-based geophysical models, the principal characteristics of each unit are summarized in the following four subsections.

7.5.1. Current Okavango Delta (OD)

The lithologies and hydrological conditions of the current Okavango Delta sediments are spatially variable, ranging from dry and freshwater-saturated sand in most regions of the delta to clay and thick salt accumulations on many small islands. Highly variable moderate to high resistivities in the upper parts of our models reflect the heterogeneity of the lithologies and hydrological conditions. Seismic velocities of the dry and water-saturated sediments are very low and low, respectively. Except for reflectors that likely represent buried river channel deposits at one site, shallow parts of the seismic sections are practically featureless.

7.5.2. Paleo Lake Makgadikgadi (PLM)

The relatively homogeneous conductive layer in our TEM and HTEM models is interpreted as a northwesterly extension of the PLM sedimentary unit. Surface evidence for PLM is observed in a large area that encompasses Lake Ngami, the Mababe Depression, and the Makgadikgadi Basin (Burrough et al., 2009a, and references therein). Its resistivity and upper and lower boundaries are well defined by the resistivity models for the HR2, Wheat Fields, and Golf Course sites. Low seismic P-wave velocities support the interpretation of the conductive layer as a sedimentary unit. The low resistivity is best explained by a combination of saline-water-saturated sand and clay. There are numerous deep saline groundwater samples (>3000 mg/l TDS) along the western edge of the delta (T. Preston, personal communication). Based on their depths and high clay contents, the sediments intersected in the lower parts of the distant boreholes are interpreted to be samples of PLM sediments.

Seismic images of PLM beneath Wheat Fields and Golf Course contain subhorizontal layered reflectors, in particular towards the base of the unit, which together with the low resistivities are consistent with sediments deposited in a lake. Strong seismic reflectors coincide with the relatively sharp transition from the conductive PLM unit to the more resistive POM unit below.

According to the low resistivity values between depths of 50 and 100 m in the HTEM model of Fig. 2b and c, the PLM unit extends beneath the entire current megafan covered by the HTEM survey. Since low apparent resistivities are also observed in the late time gates of HTEM data recorded directly south of our HTEM survey area (Campbell et al., 2006), PLM sediments are probably continuous beneath the entire delta south of the panhandle. As a consequence, the total area once covered by PLM increases from Burrough et al.'s (2009a) estimate of 66,000 km^2 to at least 90,000 km^2, making it larger than any lake on Earth today (Podgorski et al., 2013b).

7.5.3. Paleo Okavango Megafan (POM)

Low P-wave velocities and subhorizontal layered reflectors require the moderately to highly resistive unit beneath the PLM conductive unit at Jao, Wheat Fields, and Golf Course to be sedimentary. The resistivities require it to be a freshwater-saturated predominantly sand-rich unit. Substantial salt in the water or significant clay- or silt-rich components are not compatible with the resistivity estimates (Milzow et al., 2009). The upper boundary of the unit is well resolved by the marked increases in resistivity at the base of the conductive layer in the TEM and HTEM models, and its lower boundary is the well determined sediment–basement contact (Fig. 16). At Wheat Fields and Golf Course, particularly prominent reflectors are observed at its upper boundary and large increases in resistivity are inferred at its lower boundary. It is highly unlikely that sediments from this unit have been sampled in any of the distant boreholes.

Freshwater-saturated units underlying saline-water aquifers might seem unusual, but it is a common occurrence in sedimentary basins and deltas on continental shelves throughout the globe (Post et al., 2013). Analogous to the offshore examples, we presume that relatively dense saline water within the PLM sediments is prevented from sinking into the POM unit by largely impermeable clay units of the PLM unit.

The primary justification for Podgorski et al.'s (2013b) interpretation of this sedimentary unit as the remnants of a paleo megafan (POM) or paleo inland delta is its distinct fan shape in the horizontal plane (Fig. 2e and f) and its semi-conical shape in three dimensions (Fig. 17). This interpretation is supported by the combination of sedimentary layering and the unit's moderate to high resistivity. Although lacustrine and overbank deposits are invariably layered, they are usually dominated by low resistive silt- and clay-rich sediments.

The maximum extent of POM in Fig. 2f and the depth contours in Fig. 17 are defined by the volume of material with resistivities between 40 and 300 Ω m. Our resistivity and P-wave velocity models indicate
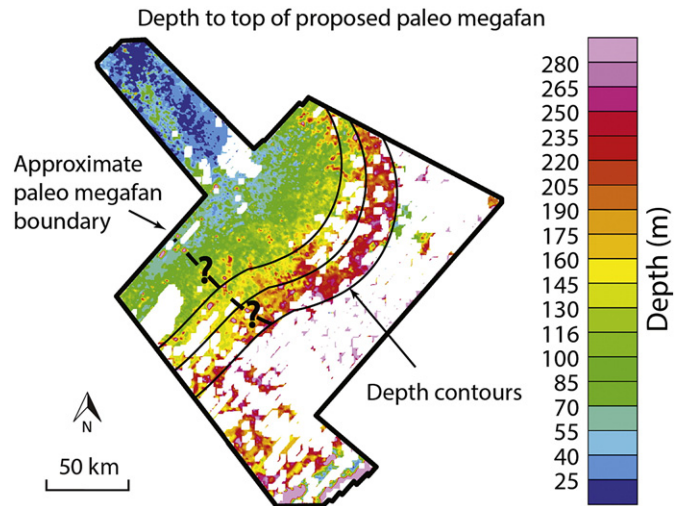

Depth to top of proposed paleo megafan

Fig. 17. Depth of postulated POM as defined by the 40–300 Ω m layer in the HTEM data. Its southwestern boundary is only poorly resolved. Modified from Podgorski et al. (2013b).

that PLM sediments lie directly on basement at HR2; there are no POM sediments beneath this site. For this reason, the outline of the POM unit is truncated along a poorly delineated line on its southwestern margin. The total area of the POM unit in Fig. 2f is about 8550 km^2, about a fifth the size of the current megafan (McCarthy, 2006).

7.5.4. Basement

The basement rocks are characterized by high to very high resistivities, high P-wave velocities, and featureless to highly complex seismic reflector patterns. Its upper boundary is a strong reflector.

7.6. Changing sedimentary conditions

There is insufficient information to determine what caused the depositional regimes to change at time scales relevant to (i) the generation of the individual reflections and (ii) the transition from a delta or fan environment to a lake. Water-level fluctuations have undoubtedly played a role, with a high probability that lacustrine, deltaic, fluvial (including overbank), and aeolian (including aerosols) sediments were deposited at various times. Burrough et al. (2009b, and references therein) have argued that significant variations in climate triggered the PLM water-level fluctuations in the area currently occupied by the Magkadigkadi Basin. In contrast, Moore et al. (2012) claim that PLM water-level changes in the Magkadigkadi Basin were generated by tectonic-induced redirections of major rivers. Neither our seismic reflection data nor the borehole logs provide the details necessary to determine which of these mechanisms dominated in the Okavango Delta region. However, we note that major climate variations are needed to explain water-level fluctuations inferred from high quality seismic reflection sections recorded in several East African Rift lakes and companion borehole logs (Scholz et al., 2003; McGlue et al., 2006; Lyons et al., 2011; Karp et al., 2012). Furthermore, the active fault scarp along the southeastern margin of the delta and ongoing seismicity suggest that tectonism has also played a role in determining the sedimentary environment.

8. Conclusions and recommendations

Results of ground-based geophysical investigations at four strategically located field sites have been used to refine a four-unit geological/hydrogeological model of the Okavango Delta that was originally inspired by the results of an extensive helicopter time-domain

electromagnetic (HTEM) survey of the delta. The boundaries, electrical resistivities, P-wave velocities, and seismic facies of the modern delta, Paleo Lake Makgadikgadi (PLM), and Paleo Okavango Megafan (POM) sedimentary units as well as the basement unit are generally well defined in the new physical property models and images.

Abrupt changes in P-wave velocities delineate the contacts between dry and water-saturated sediments and between water-saturated sediments and basement at all sites, and the seismic reflection sections image buried abandoned river channels within the modern delta and PLM units along the western margin of the delta and highly reflective subhorizontal sedimentary layers within the PLM and POM units in the north-central regions. Electrical resistivity variations provide strong constraints on the types of sediments and the salinity of their pore fluids.

Continuation of electrically conductive PLM sediments beneath the Okavango Delta is now firmly established. Our results suggest that sediments intersected in boreholes in the northeastern and southeastern parts of the delta are PLM deposits. With the extension of PLM beneath the Okavango Delta, its 90,000 km^2 area is larger than that of any lake on Earth today.

There is little doubt that resistive freshwater-saturated sand of the proposed POM unit lies between the PLM unit and basement. The contact between the PLM and POM units is delineated by sizeable changes in resistivity at three of the sites and by prominent seismic reflections at two of the sites. Impermeable clay layers that comprise major components of the PLM unit are preventing its saline pore waters from sinking into the underlying units.

The paleo megafan or paleo deltaic origin of the freshwater-saturated sand unit is based on its fan shape in horizontal plan view and semiconical shape in three dimensions. Continuous subhorizontal reflections within the unit are consistent with this interpretation. Morphologically, this unit would be a paleo megafan or paleo inland delta depending on the absence or presence of a terminal lake.

Our results have demonstrated the utility of seismic reflection surveying within the Okavango Delta; the reflection sections contain important images of sedimentary features at several depth levels. Much longer continuous seismic reflection profiling should now be considered. Seismic surveying long profiles on land would be logistically challenging and extremely costly. A significantly less expensive alternative would be lake and river-based seismic surveying. We suggest that a campaign of continuous multichannel seismic reflection surveying along the main river channels together with geologically and geophysically logged boreholes at nearby selected locations would produce substantial improvements in our understanding of temporal and spatial variations of tectonism, climate, evapotranspiration, hydrological processes, and sedimentation in this vast region of southern Africa. Programmes of environmentally safe high-resolution seismic reflection surveying and scientific drilling have already been completed in a number of East African Rift lakes (Scholz et al., 2003; McGlue et al., 2006; Lyons et al., 2011; Karp et al., 2012) and seismic surveys along rivers have proven to be practical (Haimberger et al., 2005). The results of the lake seismic surveying and borehole logging within the East African Rift have markedly improved our knowledge of tectonism and climate variability in that part of the continent.

Acknowledgements

References

Archie, G.E., 1942. The electrical resistivity log as an aid in determining some reservoir characteristics. Trans. Am. Inst. Min. Metall. Eng. 146, 54–62.

Auken, E., Christiansen, A.V., 2004. Layered and laterally constrained 2D inversion of resistivity data. Geophysics 69, 752–761.

Auken, E., Christiansen, A.V., Jacobsen, B.H., Foged, N., Sørensen, K.I., 2005. Piecewise 1D laterally constrained inversion of resistivity data. Geophys. Prospect. 53, 497–506.

Auken, E., Pellerin, L., Christensen, N.B., Sørensen, K., 2006. A survey of current trends in near-surface electrical and electromagnetic methods. Geophysics 71, G249–G260.

Baster, I., Girardclos, S., Pugin, A., Wildi, W., 2003. High-resolution seismic stratigraphy of an Holocene lacustrine delta in western Lake Geneva (Switzerland). Eclogae Geol. Helv. 96 (Supplement 1), S11–S20.

Bauer, P., 2004. Flooding and Salt Transport in the Okavango Delta, Botswana: Key Issues for Sustainable Wetland Management. (Ph.D. dissertation). ETH Zurich.

Bräuer, B., Ryberg, T., Lindeque, A., 2007. Shallow seismic velocity structure of the Karoo Basin, South Africa. S. Afr. J. Geol. 110, 439–448.

Brunner, P., Hendricks Franssen, H.-J., Kgotlhang, L., Bauer-Gottwein, P., Kinzelbach, W., 2007. How can remote sensing contribute in groundwater modeling? Hydrogeol. J. 15, 5–18.

Büker, F., Green, A.G., Horstmeyer, H., 1998. Shallow seismic reflection study of a glaciated valley. Geophysics 63, 1395–1407.

Burke, K., Gunnell, Y., 2008. The African erosion surface: a continental scale synthesis of geomorphology, tectonics, and environmental change over the past 180 million years. Geol. Soc. Am. Mem. 201.

Burrough, S.L., Thomas, D.S.G., Bailey, R.M., 2009a. Mega-Lake in the Kalahari: a Late Pleistocene record of the Palaeolake Makgadikgadi system. Quat. Sci. Rev. 28, 1392–1411.

Burrough, S.L., Thomas, D.S.G., Singarayer, J.S., 2009b. Late Quaternary hydrological dynamics in the Middle Kalahari: forcing and feedbacks. Earth Sci. Rev. 96, 313–326.

Campbell, G., Johnson, S., Bakaya, T., Kumar, H., Nsatsi, J., 2006. Airborne geophysical mapping of aquifer water quality and structural controls in the Lower Okavango Delta, Botswana. S. Afr. J. Geol. 109, 475–494.

Christiansen, A.V., Auken, E., Sørensen, K., 2009. The transient electromagnetic method. In: Kirsch, R. (Ed.), Groundwater Geophysics. Springer, New York, pp. 179–226.

Cooke, H.J., 1980. Landform evolution in the context of climatic change and neotectonism in the middle Kalahari of north central Botswana. Trans. Inst. Br. Geogr. 5, 80–99.

Cox, K.G., 1989. The role of mantle plumes in the development of continental drainage patterns. Nature 342, 873–877.

Du Toit, A.L., 1927. The Kalahari and some of its problems. S. Afr. J. Sci. 24, 88–101.

Fairhead, J.D., Girdler, R.W., 1971. The seismicity of Africa. Geophys. J. R. Astron. Soc. 24, 271–301.

Garstang, M., Ellery, W.N., McCarthy, T.S., Scholes, M.C., Scholes, R.J., Swap, R.J., Tyson, P.D., 1998. The contribution of aerosol- and water-borne nutrients to the functioning of the Okavango Delta ecosystem, Botswana. S. Afr. J. Sci. 94, 215–222.

Gieske, A., 1996. Vegetation driven groundwater recharge below the Okavango Delta (Botswana) as a solute sink mechanism: an indicative model. Botsw. J. Earth Sci. 3, 33–37.

Gomez-Trevino, E., Edwards, R.N., 1983. Electromagnetic sounding in the sedimentary basin of southern Ontario—a case history. Geophysics 48, 311–330.

Greenwood, P.G., Carruthers, R.M., 1973. Geophysical Surveys in the Okavango Delta. Report 15Inst. Geol. Sci. Geophys. Div., London.

Gumbricht, T., McCarthy, T.S., Bauer, P., 2005. The micro-topography of the wetlands of the Okavango Delta, Botswana. Earth Surf. Process. Landf. 30, 27–39.

Haddon, I.G., McCarthy, T.S., 2005. The Mesozoic–Cenozoic interior sag basins of Central Africa: the Late-Cretaceous–Cenozoic Kalahari and Okavango basins. J. Afr. Earth Sci. 43, 316–333.

Haimberger, R., Hoppe, A., Schäfer, A., 2005. High-resolution seismic survey on the Rhine River in the northern Upper Rhine Graben. Int. J. Earth Sci. 94, 657–668.

Harinarayana, T., 1999. Combination of EM and DC measurements for upper crustal studies. Surv. Geophys. 20, 257–278.

Hutchison, I.P.G., Midgley, D.C., 1973. A mathematical model to aid management of outflow from the Okavango swamp, Botswana. J. Hydrol. 19, 92–112.

Jørgensen, F., Scheer, W., Thomsen, S., Sonnenborg, T.O., Hinsby, K., Wiederhold, H., Schamper, C., Burschil, T., Roth, B., Kirsch, R., Auken, E., 2012. Transboundary geophysical mapping of geological elements and salinity distribution critical for the assessment of future sea water intrusion in response to sea level rise. Hydrol. Earth Syst. Sci. Discuss. 9, 2629–2674.

Kalscheuer, T., Blake, S., Podgorski, J.E., Wagner, F., Green, A.G., Maurer, H., Jones, A.G., Muller, M., Ntibinyane, O., Tshoso, G., 2015. New insights into the hydrological system beneath the central Okavango Delta (Botswana) from joint inversions of three types of electromagnetic data explicitly constrained by seismic observations. Geophys. J. Int. (in revision).

Karp, T., Scholz, C.A., McGlue, M.M., 2012. Structure and stratigraphy of the Lake Albert Rift, East Africa: observations from seismic reflection and gravity data. AAPG Mem. 95, 299–318.

Key, R.M., Ayers, N., 2000. The 1998 edition of the National Geological Map of Botswana. J. Afr. Earth Sci. 30, 427–451.

Kinabo, B.D., Atekwana, E.A., Hogan, J.P., Modisi, M.P., Wheaton, D.D., Kampunzu, A.B., 2007. Early structural development of the Okavango rift zone, NW Botswana. J. Afr. Earth Sci. 48, 125–136.

Kinabo, B.D., Hogan, J.P., Atekwana, E.A., Abdelsalam, M.G., Modisi, M.P., 2008. Fault growth and propagation during incipient continental rifting: insights from a

combined aeromagnetic and Shuttle Radar Topography Mission digital elevation model investigation of the Okavango Rift Zone, northwest Botswana. Tectonics 27, TC3013.

Kirkegaard, C., Sonnenborg, T.O., Auken, E., Jorgensen, F., 2011. Salinity distribution in heterogeneous coastal aquifers mapped by airborne electromagnetics. Vadose Zone J. 10, 125–135.

Knight, R.J., Endres, A.L., 2005. An introduction to rock physics principles for near-surface geophysics. In: Butler, D.K. (Ed.), Near-surface Geophysics vol. 3. SEG, Tulsa, OK, pp. 31–65.

Lanz, E., Maurer, H., Green, A.G., 1998. Refraction tomography over a buried waste disposal site. Geophysics 63, 1414–1433.

Loke, M.H., Barker, R.D., 1996. Rapid least-squares inversion of apparent resistivity pseudosections by a quasi-Newton method. Geophys. Prospect. 44, 131–152.

Lyons, R.P., Scholz, C.A., Buoniconti, M.B., Martin, M.R., 2011. Late Quaternary stratigraphic analysis of the Lake Malawi Rift, East Africa: an integration of drill-core and seismic-reflection data. Palaeogeogr. Palaeoclimatol. Palaeoecol. 303, 20–37.

Mallick, K., Verma, R.K., 1979. Time-domain electromagnetic sounding computation of multi-layer response and the problem of equivalence in interpretation. Geophys. Prospect. 27, 137–155.

Mandl, G., 1981. Gravitational gliding in deltas. Geol. Soc. Lond. Spec. Publ. 9, 41–51.

McCarthy, T.S., 2006. Groundwater in the wetlands of the Okavango Delta, Botswana, and its contribution to the structure and function of the ecosystem. J. Hydrol. 320, 264–282.

McCarthy, T.S., 2013. The Okavango Delta and its place in the geomorphological evolution of southern Africa. S. Afr. J. Geol. 116, 1–54.

McCarthy, T.S., Ellery, W.N., 1994. The effect of vegetation on soil and ground water chemistry and hydrology of islands in the seasonal swamps of the Okavango Fan, Botswana. J. Hydrol. 154, 169–193.

McCarthy, T.S., Ellery, W.N., Rogers, K.H., Cairncross, B., Ellery, K., 1986. The roles of sedimentation and plant growth in changing flow patterns in the Okavango Delta, Botswana. S. Afr. J. Sci. 82, 579–584.

McCarthy, T.S., Green, R.W., Franey, N.J., 1993. The influence of neo-tectonics on water dispersal in the northeastern regions of the Okavango swamps, Botswana. J. Afr. Earth Sci. 17, 23–32.

McCarthy, T.S., Barry, M., Bloem, A., Ellery, W.N., Heister, H., Merry, C.L., Rüther, H., Sternberg, H., 1997. The gradient of the Okavango fan, Botswana, and its sedimentological and tectonic implications. J. Afr. Earth Sci. 24, 65–78.

McCarthy, T.S., Bloem, A., Larkin, P.A., 1998a. Observations on the hydrology and geohydrology of the Okavango Delta. S. Afr. J. Geol. 101, 101–117.

McCarthy, T.S., Ellery, W.N., Bloem, A., 1998b. Some observations on the geomorphological impact of hippopotamus (Hippopotamus amphibius L.) in the Okavango Delta, Botswana. Afr. J. Ecol. 36, 44–56.

McGlue, M.M., Scholz, C.A., Karp, T., Ongodia, B., Lezzar, K.E., 2006. Facies architecture of flexural margin lowstand delta deposits in Lake Edward, East African Rift: constraints from seismic reflection imaging. J. Sediment. Res. 76, 942–958.

Meier, P., Kalscheuer, T., Podgorski, J.E., Kgotlhang, L., Green, A.G., Greenhalgh, S., Rabenstein, L., Doetsch, J., Kinzelbach, W., Auken, E., Mikkelsen, P., Foged, N., Jaba, B.C., Tshoso, G., Ntibinyane, O., 2014. Hydrogeophysical investigations in the western and north-central Okavango Delta (Botswana) based on helicopter and ground-based transient electromagnetic data and electrical resistance tomography. Geophysics 79, B201–B211.

Miall, A.D., 1985. Architectural-element analysis: a new method of facies analysis applied to fluvial deposits. Earth Sci. Rev. 22, 261–308.

Milzow, C., Kgotlhang, L., Bauer-Gottwein, P., Meier, P., Kinzelbach, W., 2009. Regional review: the hydrology of the Okavango Delta, Botswana—processes, data and modelling. Hydrol. J. 17, 1297–1328.

MMEWR (Ministry of Minerals, Energy and Water Resources), 2004. DWA Maun Groundwater Development Project: Phase 2, Resources Assessment and Wellfield Development: Final Report. Botswana Department Water Affairs, Gaborone, Botswana (27 pp.).

Modisi, M.P., Atekwana, E.A., Kampunzu, A.B., Ngwisanyi, T.H., 2000. Rift kinematics during the incipient stages of continental extension: evidence from the nascent Okavango rift basin, northwest Botswana. Geology 28, 939–942.

Moore, A.E., Larkin, P.A., 2001. Drainage evolution in south-central Africa since the break-up of Gondwana. S. Afr. J. Geol. 104, 47–68.

Moore, A.E., Cotterill, F.P.D., Eckardt, F.D., 2012. The evolution and ages of Makgadikgadi palaeo-lakes: consilient evidence from Kalahari drainage evolution. S. Afr. J. Geol. 115, 385–413.

Nyboe, N.S., Jørgensen, F., Sørensen, K.I., 2010. Integrated inversion of TEM and seismic data facilitated by high penetration depths of a segmented receiver setup. Near Surf. Geophys. 8, 467–473.

Oldenburg, D.W., Li, Y.G., 1999. Estimating depth of investigation in dc resistivity and IP surveys. Geophysics 64, 403–416.

Podgorski, J.E., Auken, E., Schamper, C., Christiansen, A.V., Kalscheuer, T., Green, A.G., 2013a. Processing and inverting commercial helicopter time-domain electromagnetic data for environmental assessments and geological and hydrological mapping. Geophysics 78, E149–E159.

Podgorski, J.E., Green, A.G., Kgotlhang, L., Kinzelbach, W.K.H., Kalscheuer, K., Auken, E., Ngwisanyi, T., 2013b. Paleo megalake and paleo megadelta in southern Africa. Geology G34735-1.

Post, V.E.A., Groen, J., Kooi, H., Person, M., Ge, S., Edmunds, W.M., 2013. Offshore fresh groundwater reserves as a global phenomenon. Nature 2013, 71–78.

Prior, D.B., Coleman, J.M., 1984. Submarine slope instability. In: Brunsen, D., Prior, D.B. (Eds.), Slope Instability. John Wiley & Sons, Hoboken, NJ, pp. 419–455.

Raiche, A.P., Jupp, D., Rutter, H., Vozoff, K., 1985. The joint use of coincident loop transient electromagnetic and Schlumberger sounding to resolve layered structures. Geophysics 50, 1618–1627.

Reeves, C.V., 1972. Rifting in the Kalahari. Nature 237, 95–96.

Reiser, F., Podgorski, J., Schmelzbach, C., Horstmeyer, H., Green, A.G., Kalscheuer, T., Maurer, H., Kinzelbach, W., Gomotsang, T., 2014. Constraining helicopter electromagnetic models of the Okavango Delta with seismic-refraction and seismic-reflection data. Geophysics 79, B123–B134.

Schmelzbach, C., Zelt, C.A., Juhlin, C., Carbonell, R., 2008. P- and SV-velocity structure of the South Portuguese Zone fold-and-thrust belt, SW Iberia, from traveltime tomography. Geophys. J. Int. 175, 689–712.

Scholz, C.A., 1995. Deltas of the Lake Malawi Rift, East Africa: seismic expression and exploration implications. AAPG Bull. 79, 1679–1697.

Scholz, C.H., Koczynski, T.A., Hutchins, D.G., 1976. Evidence for incipient rifting in Southern Africa. Geophys. J. R. Astron. Soc. 44, 135–144.

Scholz, C.A., King, J.W., Ellis, G.S., Swart, P.K., Stager, J.C., Colman, S.M., 2003. Paleolimnology of Lake Tanganyika, East Africa, over the past 100 kyr. J. Paleolimnol. 30, 139–150.

Siemon, B., Steuer, A., Ullmann, A., Vasterling, M., Voß, W., 2011. Application of frequency-domain helicopter-borne electromagnetic for groundwater exploration in urban areas. Phys. Chem. Earth 36, 1373–1385.

Spies, B.R., Frischknecht, F.C., 1991. Electromagnetic sounding. In: Nabighian, M.N. (Ed.), Electromagnetic Methods in Applied Geophysics vol. 2. SEG, Tulsa, pp. 285–425.

Stanistreet, I.G., McCarthy, T.S., 1993. The Okavango Fan and the classification of subaerial fan systems. Sediment. Geol. 85, 115–133.

Steuer, A., Siemon, B., Auken, E., 2009. A comparison of helicopter borne electromagnetic in frequency- and time-domain at the Cuxhaven valley in Northern Germany. J. Appl. Geophys. 67, 194–205.

Stümpel, H., Kähler, S., Meissner, R., Milkereit, B., 1984. The use of seismic shear waves and compressional waves for lithological problems of shallow sediments. Geophys. Prospect. 32, 662–675.

Thomas, D.S.G., Shaw, P.A., 1988. Late Cainozoic drainage evolution in the Zambezi Basin: geomorphological evidence from the Kalahari rim. J. Afr. Earth Sci. 7, 611–618.

Thomas, D.S.G., Shaw, P.A., 1991. The Kalahari Environment. Cambridge University Press, Cambridge, U.K.

Viezzoli, A., Christiansen, A.V., Auken, E., Sørensen, K., 2008. Quasi-3D modeling of airborne TEM data by spatially constrained inversion. Geophysics 73, F105–F113.

Wood, S.H., 1994. Seismic expression and geological significance of a lacustrine delta in Neogene deposits of the Western Snake River Plain, Idaho. AAPG Bull. 78, 102–121.